A Modeling Study of the Relative Roles of Tropical and Extratropical SST Anomalies in the Variability of the Global Atmosphere–Ocean System

NGAR-CHEUNG LAU AND MARY JO NATH

Geophysical Fluid Dynamics Laboratory/NOAA, Princeton University, Princeton, New Jersey

(Manuscript received 24 August 1993, in final form 16 November 1993)

ABSTRACT

In three parallel experiments, an atmospheric general circulation model has been subjected to observed, monthly varying sea surface temperature (SST) conditions in each of the following domains: near-global ocean (GOGA run), tropical Pacific (TOGA run), and midlatitude North Pacific (MOGA run). Four independent realizations were obtained for the model response to the sequence of SST anomalies during the 1946–88 period in each of the above regions.

The principal modes of coupling between the imposed SST forcing and the simulated Northern Hemisphere wintertime 515-mb height field in various experiments have been identified using a singular value decomposition (SVD) procedure. The leading SVD mode for the GOGA experiment is qualitatively similar to that based on observational data, although the amplitudes of the simulated height anomalies are notably lower than the observed values. The SST pattern of this mode resembles that associated with El Niño events. The accompanying 515-mb height anomaly is dominated by a wavelike pattern in the North Pacific/North American sector. The TOGA experiment reproduces many of the atmosphere–ocean relationships discerned from the GOGA output. Conversely, the MOGA run yields a much weaker and less reproducible response. The contrast between the TOGA and MOGA runs is indicative of the primacy of tropical Pacific SST anomalies in forcing the midlatitude atmospheric circulation.

In the TOGA experiment, the remote atmospheric responses to tropical Pacific SST anomalies influence the energy exchange across the local air–sea interface, and could thereby perturb the SST field outside of the tropical Pacific. Through this "atmospheric bridge," the tropical Pacific could set the pace for variability of the global ocean. Analysis of the TOGA output indicates that, over the North Pacific, changes in the surface energy fluxes are mainly determined by the surface wind speed and by the strength of temperature and moisture advection. Over the Indian Ocean, variations in the incident solar radiation due to changes in cloud cover also affect the surface fluxes. The worldwide SST tendencies inferred from the variations in surface fluxes simulated in the TOGA experiment are in good agreement with the local observed SST anomalies.

1. Introduction

In many recent investigations of large-scale air–sea interaction, an issue of critical importance is the role of sea surface temperature (SST) anomalies at different geographical sites in the variability of the atmospheric circulation. The empirical evidence relevant to this problem may be summarized as follows:

• *Tropical SST anomalies are correlated with the midlatitude atmosphere*

The link between tropical Pacific SST variations, such as those accompanying El Niño–Southern Oscillation (ENSO) episodes, and a characteristic atmospheric pattern in the North Pacific/North American sector has been demonstrated in many observational studies (van Loon and Madden 1981; Horel and Wallace 1981; among others). These results support the findings based on simple mechanistic models (e.g., Hoskins and Karoly 1981; Sardeshmukh and Hoskins 1988), which indicate that the midlatitude atmosphere could respond remotely to heat sources and sinks in the Tropics.

• *Extratropical SST anomalies are correlated with the midlatitude atmosphere*

Well-defined relationships between midlatitude atmospheric patterns and the in situ SST anomalies in the extratropical North Pacific and North Atlantic have been documented by Namias (1969), Davis (1976), Ratcliffe and Murray (1970), and Wallace et al. (1990), among others. The time lag analyses performed by some of the above authors indicate that the atmospheric changes typically occur one to several months *in advance of* the midlatitude SST changes, thus suggesting that extratropical SST variability could be a response to atmospheric driving.

• *SST anomalies at different maritime sites are correlated with each other*

The connection between SST anomalies in the tropical Pacific and those in the North Pacific has been

Corresponding author address: Dr. Ngar-Cheung Lau, Geophysical Fluid Dynamics Laboratory/NOAA, Princeton University, P.O. Box 308, Princeton, NJ 08542.

noted by Weare et al. (1976). The results presented by Hsiung and Newell (1983) and Pan and Oort (1983, 1990) indicate that the ENSO signal in the tropical Pacific is part of a global-scale SST pattern, with anomaly centers scattering throughout the World Ocean.

The above relationships between the atmospheric and oceanic fields in various latitude zones pose the following questions:

- What is the relative importance of tropical and extratropical SST anomalies in forcing the midlatitude atmospheric circulation?
- How do the *local* atmosphere–ocean feedbacks within the extratropics differ from the *remote* interaction between the midlatitude atmosphere and tropical SST anomalies?
- What are the processes responsible for the links between seasonal SST anomalies at distant geographical sites? What is the role of the atmospheric circulation in such basin- and global-scale teleconnections in the SST field?

Since most of the feedback mechanisms operate simultaneously in the real climate system, it is difficult to resolve the above issues in an unambiguous manner using observational data alone. A complementary approach is to isolate subsets of such processes in the controlled settings of general circulation model (GCM) experiments. The response of the model atmosphere to ENSO-related SST anomalies in the tropical Pacific has been examined by Blackmon et al. (1983), Shukla and Wallace (1983), and Lau (1985), among others. The impact of midlatitude SST anomalies on the simulated atmosphere has been investigated by Palmer and Sun (1985), Pitcher et al. (1988), and Kushnir and Lau (1992). The modeling studies by Pitcher et al. (1988), Lau and Nath (1990), Barnett et al. (1991), and Graham et al. (1994) have considered tropical SST anomalies in conjunction with extratropical SST changes.

The primary goal of the present study is to offer a more definitive account of the nature of atmospheric interactions with various SST sites. We will conduct a larger array of experiments than was attempted in Lau and Nath (1990). Included in these new experiments are runs subjected to tropical SST anomalies only, to extratropical SST anomalies only, and to a combination of tropical and extratropical SST forcings. The duration of each run is extended from the 30-yr period used in Lau and Nath (1990) to a 43-yr period. Multiple integrations are performed for each scenario of SST forcing so as to minimize uncertainties due to sampling fluctuations.

The main analysis tools and some important empirical relationships between the SST and atmospheric fields are reviewed in sections 2 and 3. The design of the suite of GCM experiments is described in section 4. The principal coupled modes of variability in different model runs are compared in sections 5 and 6. Evidence is then presented in section 7 on the role of the atmospheric circulation as an intermediary between the ENSO-related SST signal in the tropical Pacific and SST changes elsewhere in the World Ocean.

2. Analysis tools

Singular value decomposition (SVD) is a method for identifying the prevalent modes of coupling between two data fields. The formulation of this technique has recently been given by Bretherton et al. (1992, sections 2 and 3b), to which the interested reader is referred for further details. The application of this tool to the extratropical air–sea coupling problem has been demonstrated in a companion article by Wallace et al. (1992).

Consider two data fields that are functions of space and time and denote them as the "left" field L (consisting of N_L grid points, with the temporal variations at each grid point being represented at T different time points) and the "right" field R (consisting of N_R grid points and the same T time points). In all SVD analyses performed in this study, both L and R have been normalized to unit standard deviation. To search for pairs of spatial patterns explaining maximal mean-square temporal covariance between L and R, a singular value decomposition is performed on the $N_L \times N_R$ cross-correlation matrix between L and R. This operation yields pairs of spatial patterns p (with N_L grid points) and q (with N_R grid points) for the left and right fields, respectively.

For each pair of patterns, the time series a for the left field (with T time points, hereafter referred to as the expansion coefficients) can be constructed by computing the spatial projection of L at each time point on p. Analogously, the expansion coefficients b for the right field can be obtained by projecting R on q. The expansion coefficients a and b represent the amplitude and polarity of the characteristic patterns for the left and right fields at each of the T time points.

Following Wallace et al. (1992), the spatial structure of the SVD mode is illustrated by a pair of patterns. One of these patterns shows the geographical distribution of the temporal correlation coefficients between b and the local gridpoint data for L. The other pattern shows the correlations between a and R. These patterns, referred as the heterogeneous correlation maps by these authors, highlight those spatial features in one field that exhibit strong temporal relationships with the companion field.

The strength of coupling between the left and right fields is indicated by two measures. The first measure, to be denoted as SCF, is the fraction of the total squared covariance between L and R that is attributed to the SVD pair in question. The second, denoted as r, is the temporal correlation coefficient between a and b. The pair of heterogeneous correlation maps and the cor-

responding expansion coefficients a, b together describe a preferred coupled mode between the two data fields L and R. The SVD method generates many such modes of covariability. The relative importance of these modes is assessed by rank ordering according to the magnitude of SCF for each mode. In the present study, we will be concerned exclusively with the behavior of the leading mode (i.e., that which accounts for maximum squared covariance between L and R).

A useful measure of the significance of the heterogeneous correlation patterns themselves is given by the fraction of domain-integrated variance of R explained by a and the fraction of variance of L explained by b. This fraction for a given heterogeneous correlation map, to be denoted as VARF, may be computed by spatially averaging the squares of the gridpoint values in that map.

3. Some key observational results

a. North Pacific SST versus tropical Pacific SST

We will first analyze the relationship between SST observations in the tropical and extratropical portions of the Pacific basin using the SVD method. In the present application, the left field L is taken to be the SST data in the tropical Pacific between 25°S and 25°N, and the right field R represents the SST variations in the North Pacific between 25° and 55°N. The SST observations have been extracted from the Comprehensive Ocean Atmosphere Data Set [COADS; see documentation by Woodruff et al. (1987)]. The original 2° × 2° box averages have been objectively analyzed at the Geophysical Fluid Dynamics Laboratory (GFDL) on an 1° × 1° longitude–latitude grid, as described in Pan and Oort (1990). The latter analyses were interpolated on the Gaussian grid for the spectral GCM to be used in this study (see section 4), with a longitude–latitude resolution of 7.5° and ~4.5°. A subset of the points in this Gaussian grid has been used to perform the SVD analysis. This subset is chosen by sampling every other grid point along a given latitude, with points along neighboring rows being staggered with respect to each other. The number of grid points representing the SST fields in the tropical Pacific (N_L) and North Pacific (N_R) are 116 and 55, respectively. Throughout this paper, we will confine our attention to observed and simulated phenomena for the 1946–88 period during the northern winter season, which is defined as the average over the months of December, January, and February. The number of time points T used in this and all following SVD analyses is 42.

The leading SVD mode for the tropical and North Pacific SST fields explains 64% of the total squared covariance, and the correlation coefficient r between the pair of expansion coefficients a, b is 0.75. The heterogeneous correlation patterns for this mode are displayed in Fig. 1. The upper panel depicts the correlation between the SST data in the North Pacific R and the expansion coefficients for the tropical Pacific SST field a and explains 13% of the domain-integrated variance (VARF). The lower panel shows the correlation between the tropical Pacific SST data L and the expansion coefficients for the North Pacific SST field b, and explains 16% of the variance. Although only a subset of the grid points has been used in the SVD analysis, the patterns in Fig. 1 have been obtained by correlating a and b with all available points in the full 7.5° × ~4.5° Gaussian grid, so as to bring out more details of the spatial structure for this mode. An analogous approach has been followed in constructing all other heterogeneous correlation charts in this paper. The patterns in Fig. 1 indicate that the SST anomalies in the central–eastern tropical Pacific are correlated negatively with those in the central North Pacific and positively with fluctuations in the eastern and western North Pacific. These relationships are similar to those reported by Weare et al. (1976) on the basis of a principal component analysis of the basinwide Pacific SST field.

In order to identify those winters in which the relationships depicted in Fig. 1 are particularly strong, the expansion coefficients a, b are presented in Fig. 2. The ordinate and abscissa of this diagram correspond to the values of a and b, respectively. For most of the winters in the 1946–88 period, the pairs of expansion coefficients are represented in Fig. 2 using individual dots. Those winters in which both a and b have relatively large magnitudes of the same polarity, and that also correspond to extreme swings in the ENSO cycle (van Loon and Madden 1981; Rasmusson and Carpenter 1982), are highlighted using numerical labels. The six outstanding winters highlighted in the upper-right quadrant (i.e., the winters starting with the December of 1957, 1969, 1976, 1982, 1986, and 1987) will be referred to as "warm" winters. The six prominent winters in the lower-left quadrant (i.e., 1949, 1955, 1964, 1970, 1973, and 1975) will be referred to as "cold" winters. These warm and cold winters will be used in section 6 as the basis for constructing composites of the responses in various GCM experiments.

b. 500-mb height versus global SST

We next describe the results of another SVD analysis, in which the left field corresponds to the SST throughout the Pacific, Atlantic, and Indian Oceans between 40°S and 60°N (with 350 grid points), and the right field is taken to be the observed 500-mb height north of 20°N (with 132 grid points). The 500-mb height data were obtained from the operational analyses produced by the U.S. National Meteorological Center (NMC).

The heterogeneous correlation patterns resulting from the present SVD analysis are presented in Figs. 3a and 3b, respectively. The Pacific SST features in Fig. 3b bear a strong resemblance to those shown in Fig. 1. The same figure also shows in-phase SST vari-

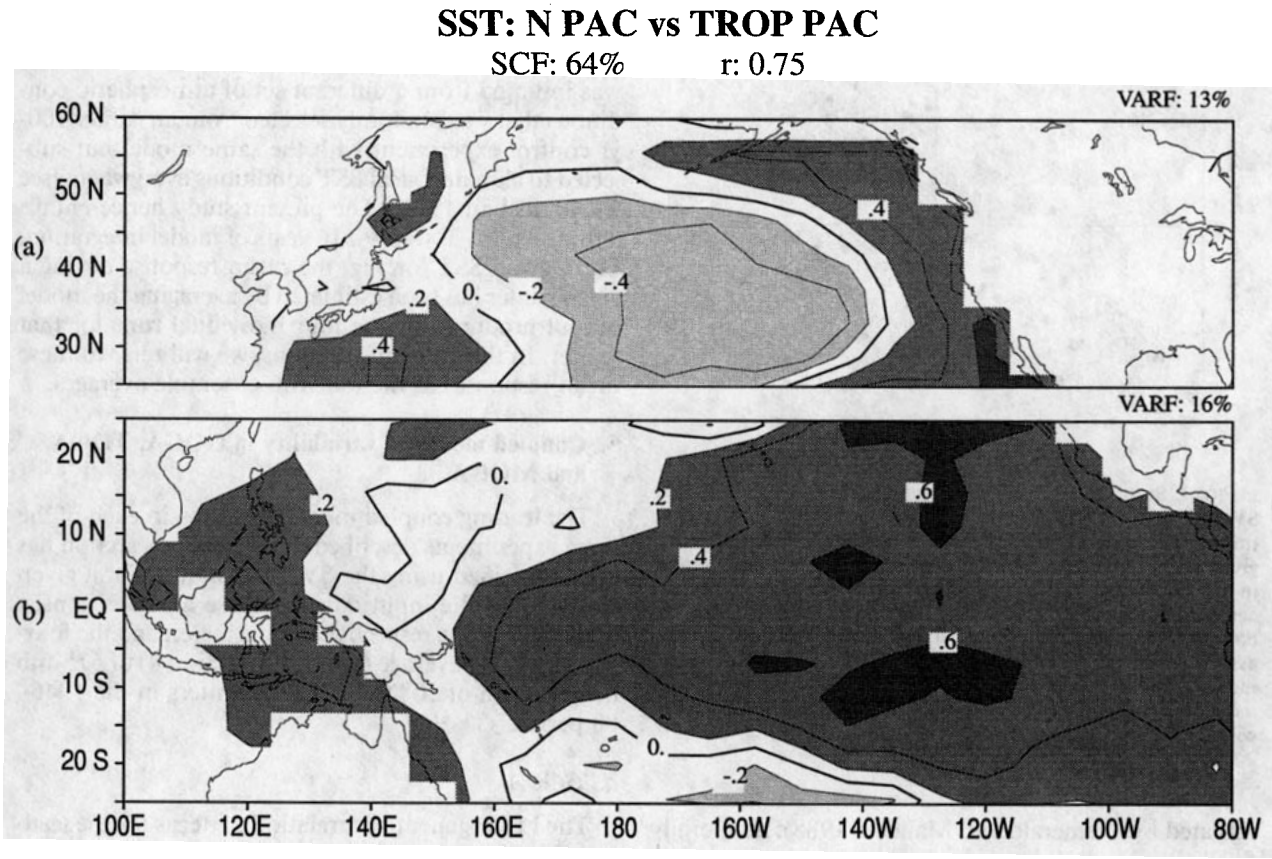

FIG. 1. Heterogeneous correlation patterns for the leading SVD mode of the observed SST field in the (a) North Pacific and (b) tropical Pacific, for the northern winter. Contour interval: 0.2. In this and all following heterogeneous correlation patterns in this paper, the squared covariance fraction (SCF) explained by the SVD mode and the temporal correlation coefficient between the pair of expansion coefficients associated with this mode (r) are given at the top center. The fraction of domain-integrated variance (VARF) explained by each heterogeneous correlation pattern is given at the upper-right corner of that pattern.

ations in the tropical Pacific, western subtropical North Atlantic, and the tropical Indian Ocean. The 500-mb height pattern (Fig. 3a) in the Western Hemisphere exhibits a notable spatial correspondence with the Pacific/North American (PNA) pattern documented by Wallace and Gutzler (1981) and Barnston and Livezey (1987). The correlation values in Fig. 3b indicate that the atmospheric PNA-like pattern is as strongly linked to the North Pacific (~ -0.6) as it is with the tropical Pacific (~ 0.6). It is therefore difficult to ascertain the relative importance of the tropical and extratropical SST changes in forcing the PNA pattern on the basis of the present analysis alone.

In Fig. 4 are shown the time series of the expansion coefficients for the observed (a) 500-mb height and (b) SST fields associated with the leading SVD mode. The outstanding warm (El Niño) and cold (La Niña) episodes in this period, as identified by various observational studies cited in the previous subsection, are highlighted in Fig. 4 using distinct stippling patterns. As expected, the pair of time series exhibits a strong correlation (recall that $r = 0.83$ for this mode). The El Niño (La Niña) winters are associated with large, positive (negative) expansion coefficients for both the 500-mb height and SST fields. In addition to the alternation between El Niño and La Niña events on timescales of several years, there exist decade-long epochs (e.g., 1946–56 and 1976–88) during which the expansion coefficients are dominated by a given polarity. The decadal anomaly during 1976–88 has come under intensive investigations recently (e.g., Nitta and Yamada 1989; Trenberth 1990; Trenberth and Hurrell 1994) and is apparently accompanied by substantial changes in the atmosphere–ocean circulations in the Pacific.

4. Design of model experiments

The GCM used in the present investigation is an updated version of that described in the earlier studies of Lau (1985) and Lau and Nath (1990). The horizontal variations in this global model are represented by spherical harmonics, with a rhomboidal truncation at 15 wavenumbers. The vertical variations are represented at nine discrete sigma levels. The most noteworthy modification in the present version of the model is the inclusion of the cloud prediction scheme for-

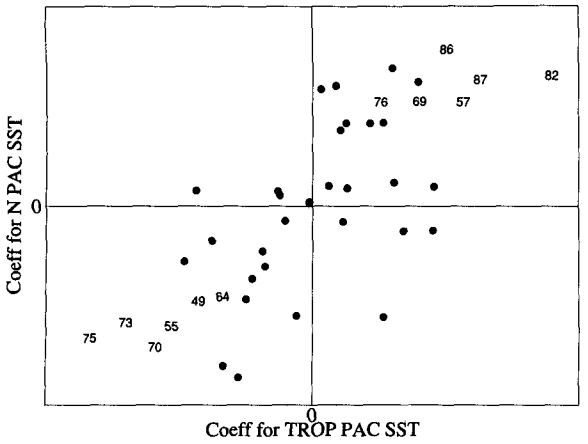

FIG. 2. Scattergram of the expansion coefficients for the leading SVD mode of the SST field in the North Pacific (ordinate) and the tropical Pacific (abscissa). The pair of expansion coefficients for a given winter is represented by either a solid dot or a two-digit number in this plot. Those winters highlighted by numerical labels are characterized by large absolute values in the expansion coefficients for both the North Pacific and tropical Pacific SST fields and are also associated with well-known warm or cold ENSO events. The numerical labels represent the last two digits of the years in which the individual outstanding winter episodes began (e.g., 82 refers to the winter of December 1982 through February 1983).

mulated by Wetherald and Manabe (1988); temporally fixed cloud cover was prescribed in the earlier studies. The observed month-to-month SST variations in selected regions, as deduced from the COADS analyses (see section 3a), were incorporated in the lower-boundary condition of the model atmosphere in the same manner as described in Lau (1985) and Lau and Nath (1990).

Three types of experiments were conducted, with each type incorporating the monthly varying SST conditions in a different geographical domain. The three domains chosen for these integrations are

- the near-global ocean between 40°S and 60°N, to be referred to as the global ocean–global atmosphere (GOGA) runs;
- the tropical Pacific between 25°S and 25°N, to be referred to as the tropical ocean–global atmosphere (TOGA) runs; and
- the North Pacific between 25° and 55°N, to be referred to as the midlatitude ocean–global atmosphere (MOGA) runs.

In all oceanic areas outside of the region of variable SST forcing for a given experiment, the lower-boundary condition has been constrained to follow the local, observed SST climatological annual cycle, with no year-to-year variability. All experiments examined here were performed for the 43-yr period from January 1946 through December 1988.

To enhance the sample size and to ascertain the reproducibility of the model response, four parallel integrations have been performed for each of the SST forcing domains listed above. Each of these four runs was initiated from a different set of atmospheric conditions that was randomly selected from an earlier 100-yr control experiment with the same model but subjected to climatological SST conditions everywhere (see Ting and Lau 1993). The present study hence entails altogether $4 \times 3 \times 43 = 516$ years of model integration. For a given SST forcing, the mean response during a given winter has been estimated by averaging the model output produced by the four individual runs for that winter. In the following sections, we will refer to these mean responses as the four-run ensemble averages.

5. Coupled modes of variability in GOGA, TOGA, and MOGA

The leading coupled mode appearing in each of the three experiments described in the previous section has been identified using the SVD technique. For a given experiment, the input data for these analyses consist of the SST in the respective forcing region and the four-run ensemble average (see end of section 4) of 515-mb height north of 20°N for the 42 winters in the 1946–88 period.

a. GOGA

The heterogeneous correlation patterns for the leading SVD mode of the (a) 515-mb height and (b) SST variations in the GOGA runs are presented in Fig. 5. In this application, the input grid for the SST forcing consists of 350 points and is identical to that used in the corresponding observational analysis in section 3. The SCF, r, and VARF values for this model mode are higher than their observational counterparts. Comparison between Figs. 3b and 5b indicates that the leading modes of air–sea coupling in both the observations and GOGA entail essentially the same global SST anomaly pattern. The observed and simulated atmospheric patterns (Figs. 3a and 5a) associated with this SST anomaly are similar in many respects. Noteworthy differences between Figs. 3a and 5a include the displacements of the simulated anomaly centers over western North America and off the eastern U.S.–Canadian seaboard from the observed positions, the stronger dipolar structure over the western Pacific in the observations, and the higher correlation values equatorward of 30°N in the GOGA result. In general, the simulated wave train acquires a more zonal orientation than the observed pattern. The characteristic atmospheric pattern in the GOGA runs exhibits a stronger temporal correlation with the tropical Pacific SST (correlation coefficients ~ 0.6) than with the central North Pacific (~ -0.4), whereas the corresponding observed correlation values are comparable in magnitude.

Temporal variations of the expansion coefficients for the (a) 515-mb height and (b) SST fields associated

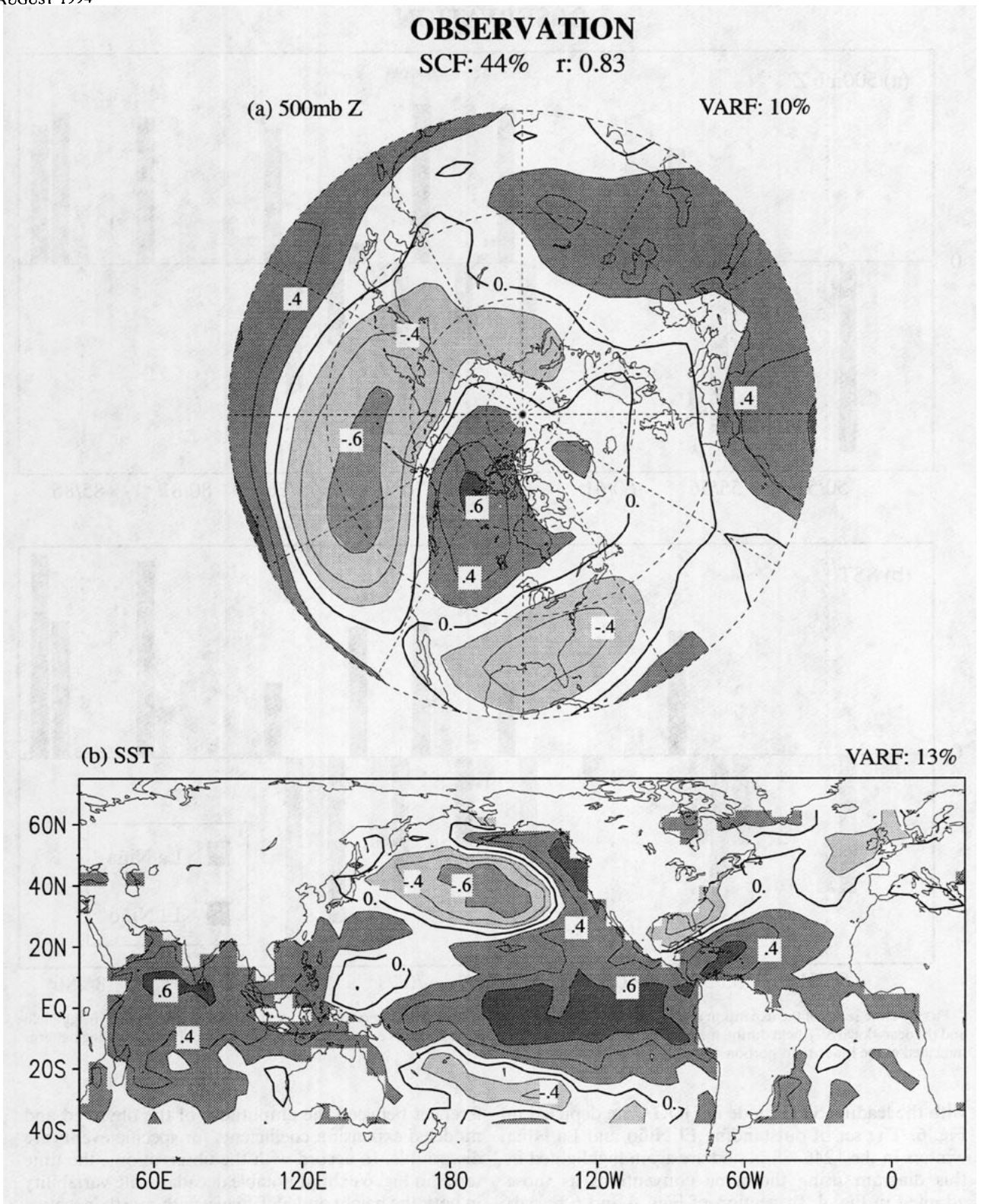

FIG. 3. Heterogeneous correlation patterns for the leading SVD mode of the observed (a) Northern Hemisphere 500-mb height field and (b) near-global SST field, during the northern winter. Contour interval: 0.2.

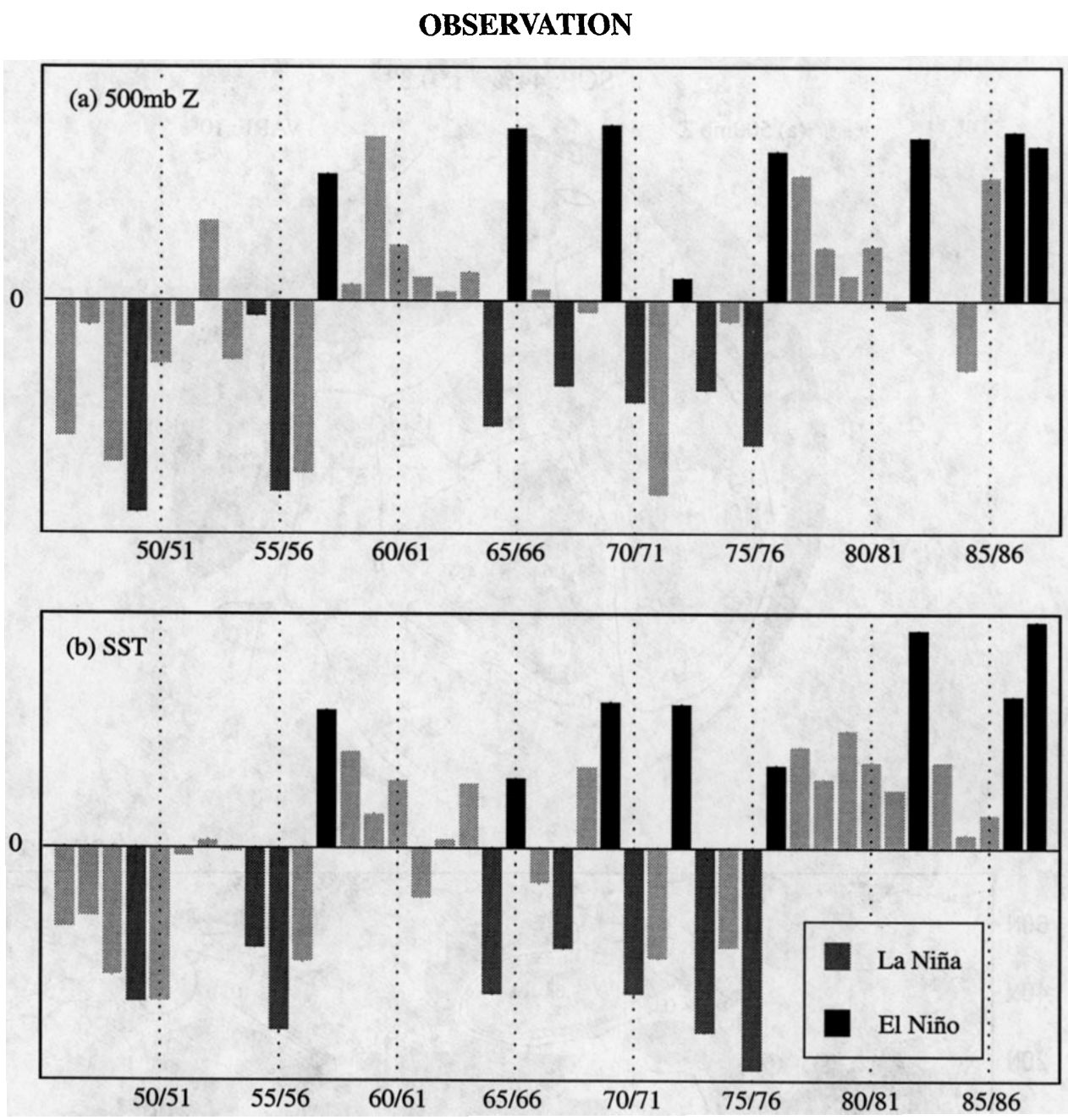

FIG. 4. Time series of the expansion coefficients for the leading SVD mode of the observed (a) Northern Hemispheric 500-mb height field and (b) near-global SST field during the northern winter. Strong El Niño and La Niña events are highlighted by the special stippling patterns indicated at the lower-right portion of (b).

with the leading SVD mode in GOGA are depicted in Fig. 6. The set of outstanding El Niño and La Niña winters in the 1946–88 period are again highlighted in this diagram using the same conventions as those adopted in Fig. 4. Inspection of Figs. 4 and 6 reveals that, without exception, the expansion coefficients for both the observed and simulated height fields are positive during the outstanding El Niño winters and negative during the La Niña episodes. However, some differences between the amplitudes of the observed and modeled expansion coefficients for specific events are discernible. In accord with the observations, the time series in Fig. 6 exhibit notable decadal-scale variability in both the height and SST fields, with mostly negative coefficients in the 1946–56 period and an abrupt transition in 1976 to a prolonged period with positive coefficients. To quantify the degree of correspondence between Figs. 4 and 6, we have computed the temporal

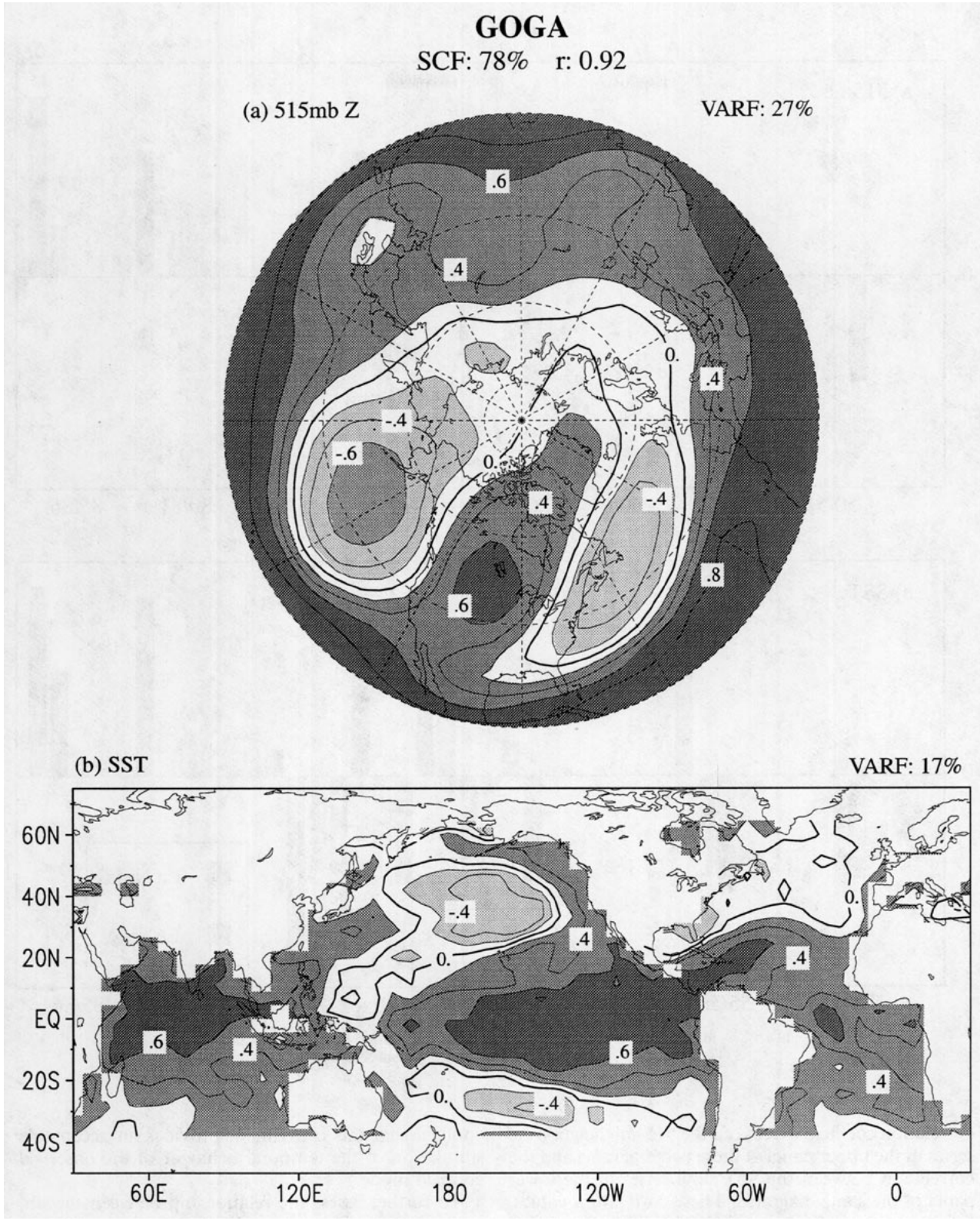

FIG. 5. As in Fig. 3 but for (a) ensemble average of the 515-mb height field simulated in the four GOGA runs and (b) the near-global SST forcing.

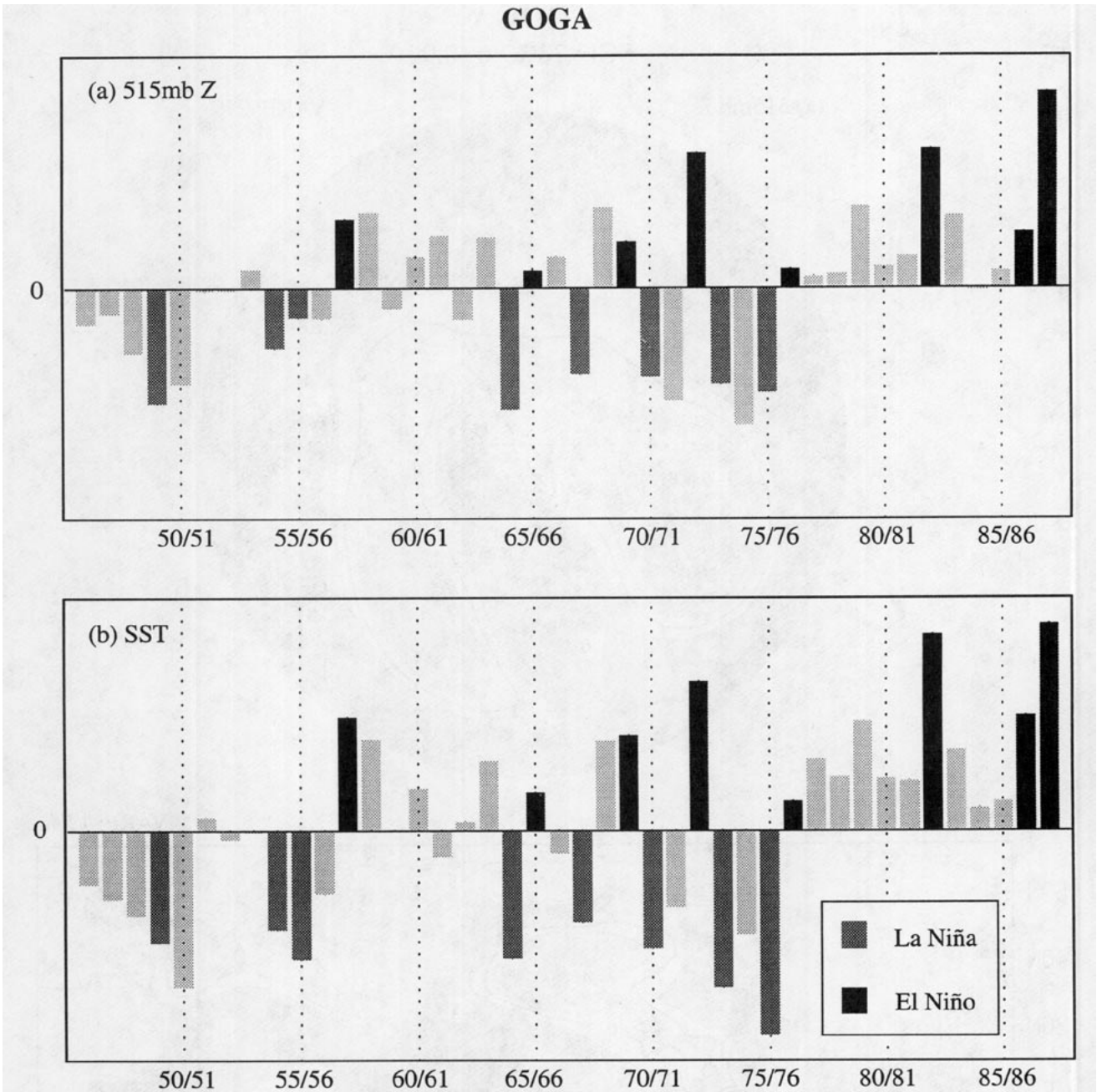

FIG. 6. As in Fig. 4 but for (a) ensemble average of the 515-mb height field simulated in the four GOGA runs and (b) the near-global SST forcing.

correlation coefficient between the 515-mb height time series in the upper panel of these two diagrams and the correlation between the SST time series in the lower panel of the same diagrams. These correlation values, together with analogous statistics for different pairings among various experiments and the observations, are summarized in Table 1. The high correlation levels between the observed and GOGA expansion coefficients (0.66 for the height field, 0.98 for the SST field) confirm that this experiment provides an acceptable simulation of the temporal behavior of the observed coupled mode.

To further assess the relationship between the observed and model-generated height anomalies, an SVD analysis has been conducted using the NMC analyses of the 500-mb height as the left field and the four-run ensemble average of 515-mb height simulated in GOGA. The SCF and r values for the leading mode

TABLE 1. Temporal correlation coefficients between the time series of expansion coefficients for the leading SVD mode of an experiment (GOGA, TOGA, or MOGA) with the corresponding time series based on observations (OBS) or another experiment. All model results are based on averages over four individual realizations for each winter. Two values are tabulated for each entry in this correlation matrix. The upper value shows the correlation between the pair of time series for the 515- or 500-mb height field. The lower value shows the correlation between the pair of time series for the SST field. The threshold correlation values corresponding to the 95% and 99% significance levels for 40 degrees of freedom are 0.26 and 0.36, respectively.

	GOGA	TOGA	MOGA
OBS	0.66	0.67	0.32
	0.98	0.93	0.77
GOGA		0.82	0.36
		0.95	0.69
TOGA			0.38
			0.58

thus obtained are 56% and 0.72, respectively. The corresponding heterogeneous correlation pattern (not shown) for the left field (NMC data) is almost identical to Fig. 3a and explains 7% of the hemispheric variance (VARF), whereas the pattern for the right field (GOGA data) resembles that shown in Fig. 5a and explains 16% of the variance. This finding indicates that the pair of patterns in Figs. 3a and 5a corresponds to the spatial structures that explain maximal temporal covariance between the observed and simulated height fluctuations. One could also infer from this result that the pattern in Fig. 5a represents the spatial manifestation of the observed PNA mode in the model atmosphere.

The SVD analysis presented in Figs. 5 and 6 has been applied separately to the output for each of the four individual GOGA runs. These results indicate that the spatial structure and temporal evolution of the leading SVD mode for the four-run ensemble average (Figs. 5–6) are well reproduced in each of the four available samples. The SCF and r values associated with the leading SVD modes for the individual runs range from ~60% to ~65% and from ~0.85 to ~0.90, respectively. The fractions of variance (VARF) explained by the heterogeneous correlation charts for the individual runs are at the ~15% level for the height field and ~16% for the SST field.

To illustrate the scatter among the 515-mb height responses in the four individual GOGA simulations, the spatial correlation coefficient R_s between the pattern shown in Fig. 5a and the height anomaly for each winter (normalized by the local standard deviation) has been computed separately for each run. The raw data values have been weighted by the square root of the cosine of latitude in these calculations. For a given spatial domain, R_s is related to the spatial mean of the products of local departures of the two fields from their respective domain averages. This statistic provides a measure of how well, and with what polarity, the simulated height pattern in a given winter projects spatially on the (time independent) pattern in Fig. 5a. To emphasize the features in the North Pacific–North America–North Atlantic sector, the domain used for computing R_s is bounded by the 30°N and 70°N latitude circles and the 150°E and 30°W meridians. The temporal variations of R_s for each of the four GOGA runs are depicted in Fig. 7 by circles. The R_s values computed using four-run ensemble averages are presented using diamonds. In analogy to Figs. 4 and 6, the outstanding El Niño and La Niña winters are identified in Fig. 7 by filling the appropriate circles and diamonds with dense and sparse stippling, respectively. The data presented in Fig. 7 demonstrate that the atmospheric response in individual winters exhibits a considerable degree of variability from one GOGA run to another. However, R_s is positive (negative) for a majority of the runs during the eight El Niño (La Niña) winters. It is also worth noting that, for a given winter, the magnitude of R_s based on four-run ensemble averages of the height data (diamonds) is noticeably larger than that obtained by averaging the four R_s values for the individual GOGA runs. This finding illustrates that the averaging process applied to the height anomalies in the four individual runs substantially reduces the noise level due to sampling fluctuations among these runs, so that R_s for the mean response (diamonds) has a larger magnitude than a majority of the corresponding values based on individual realizations (circles).

b. TOGA

In Fig. 8 is shown the heterogeneous correlation patterns associated with the leading SVD mode for (a) the four-run ensemble mean of the 515-mb height field simulated by the TOGA runs and (b) the prescribed SST forcing in the tropical Pacific. Altogether, 116 grid points have been used to represent the SST field in this case. The SCF, r, and VARF measures for the present analysis are comparable to those for the GOGA runs. Comparison among the characteristic patterns for the observations (Fig. 3), GOGA (Fig. 5), and TOGA (Fig. 8) reveals many similarities. The height anomaly center off the northeastern coast of North America is relatively less prominent in the TOGA response. The north–south dipole in the height fluctuations over the central and western North Pacific, as noted in the observations, is more evident in TOGA than in GOGA. In general, the spatial structure of the TOGA response bears a stronger resemblance to the observations than the GOGA response. However, the relatively higher amplitudes in the correlation charts for the GOGA height anomalies are closer to the corresponding observed values.

The time series of the expansion coefficients associated with the leading SVD mode for the TOGA runs

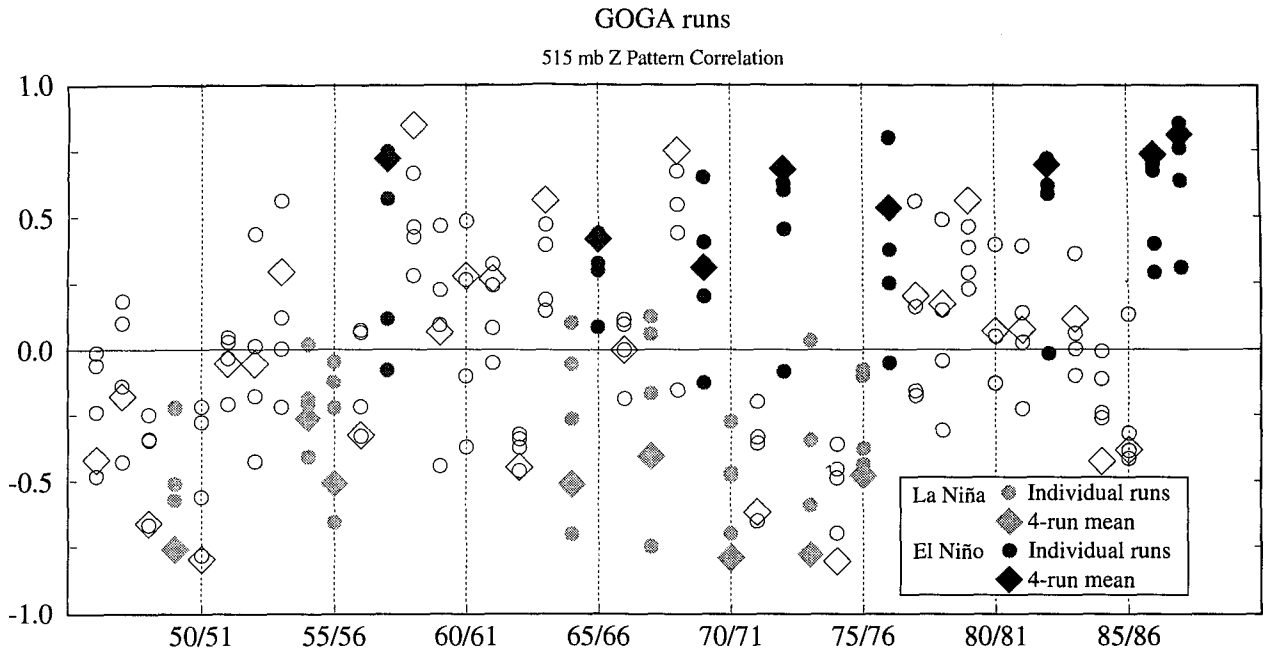

FIG. 7. Time series of the spatial correlation coefficients between the characteristic pattern of the 515-mb height field associated with the leading SVD mode for the GOGA experiment (see Fig. 5a) and the 515-mb height anomalies (normalized by local standard deviations) simulated in the same experiment during individual winters. The spatial correlation coefficients have been computed for the domain extending from 150°E eastward to 30°W and from 30° to 70°N. The results for the four different realizations of the GOGA response are depicted by circles, and those for the four-run ensemble mean are indicated by diamonds. Strong El Niño and La Niña events are highlighted by filling the circles and diamonds for the corresponding winters with stippling (see legend at lower right).

(not shown) are similar to those for the GOGA runs (Fig. 6) and the observations (Fig. 4). As shown in Table 1, the correlation coefficients between the expansion coefficients for GOGA and TOGA are 0.82 for 515-mb height and 0.95 for SST. The corresponding correlations between the TOGA and observed time series are 0.67 and 0.93. The scatter among the simulations in the four individual TOGA runs, as inferred from spatial correlation coefficients R_s (not shown) between height anomalies for each run with the pattern in Fig. 8a, is comparable to that illustrated for the GOGA runs (see Fig. 7). Again, a large majority of the individual TOGA runs yields positive (negative) R_s for the El Niño (La Niña) events.

To further evaluate the resemblance between the TOGA and GOGA responses, we have computed the spatial correlation coefficients R_s between the four-run ensemble means of the 515-mb height patterns in the GOGA and TOGA experiments for each winter. In Fig. 9, the values of R_s are plotted against the expansion coefficients for the SST field associated with the leading SVD mode in the GOGA run, which depict the amplitude and polarity of the SST anomaly pattern in Fig. 5b. The data for each winter in the 1946–88 period are represented in this figure using either a solid dot or a numerical label corresponding to the last two digits of the winter in question (adopting the same convention as in Fig. 2). The 16 winters identified by numerical labels are the outstanding warm and cold ENSO episodes highlighted in Figs. 4 and 6. It is seen that the spatial correlation between the GOGA and TOGA responses is positive in 15 of the 16 outstanding ENSO episodes.

As a measure of the performance of the TOGA experiment in reproducing the observed height anomalies during individual winters, spatial correlation coefficients R_s have been computed between the anomaly pattern for the NMC 500-mb height in a given winter and the four-run ensemble average of the 515-mb height simulated in TOGA during the same winter. In Fig. 10, these values of R_s are plotted against the expansion coefficients of the SST field associated with the leading SVD mode of atmosphere–ocean coupling in the TOGA runs (see Fig. 8), using a format similar to that in Fig. 9. It is seen that R_s is positive for all 16 El Niño or La Niña winters.

In view of the favorable comparison between the model results for TOGA and GOGA (Figs. 5, 8, and 9), as well as between TOGA and the observations (Figs. 3, 8, and 10), we are led to conclude that SST anomalies in the tropical Pacific account for most of the oceanic driving of the interannual and interdecadal variability in the simulated and observed midlatitude atmospheres.

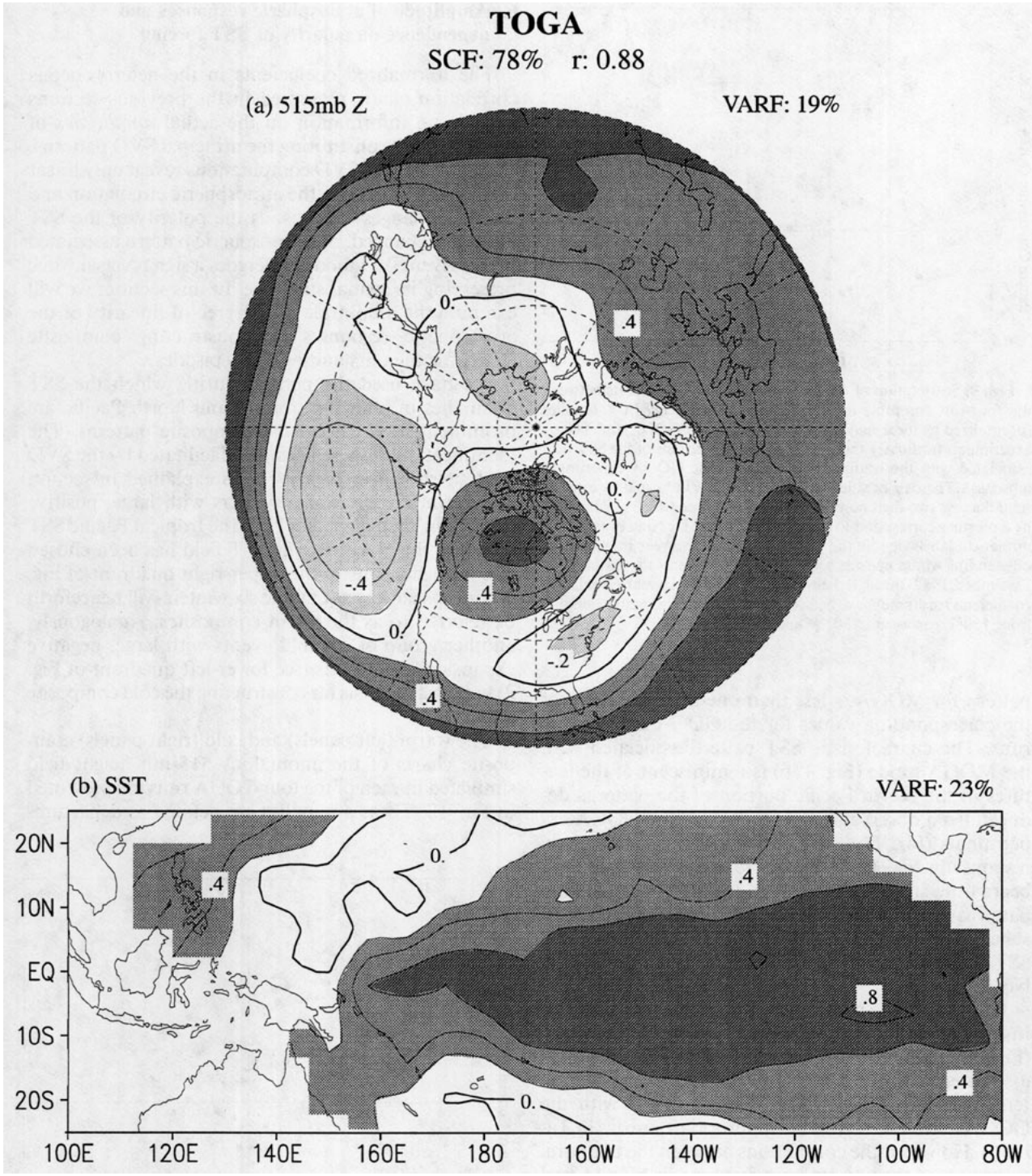

FIG. 8. As in Fig. 5 but for (a) the 515-mb height field simulated in the TOGA runs and (b) the SST forcing in the tropical Pacific.

c. MOGA

The heterogeneous correlation patterns for the leading SVD mode computed using the output from the MOGA experiments are displayed in Fig. 11. The domain of the SST field for the forcing region in the extratropical North Pacific is composed of 55 grid points. The SCF for this MOGA mode (33%) is less than half of the corresponding values for the GOGA and TOGA experiments. The r value for MOGA (0.57) is much weaker than its counterpart for GOGA and TOGA. The fraction of variance explained by the SST (height)

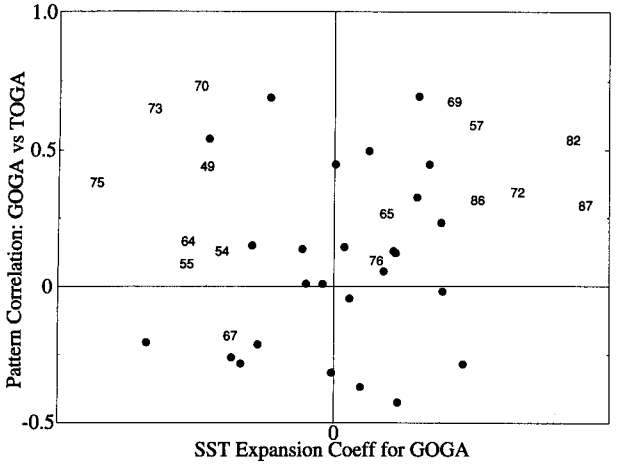

FIG. 9. Scattergram of the spatial correlation coefficients between the four-run ensemble averages of the 515-mb height anomalies (normalized by local standard deviations) in the GOGA and TOGA experiments (ordinate) and the expansion coefficients of the SST field associated with the leading SVD mode in the GOGA experiment (abscissa). The pair of values for each winter is indicated by either a solid dot or a two-digit number in this plot. Those winters highlighted by a number correspond to strong El Niño and La Niña events. The numerical labels denote the last two digits of the year in which the outstanding winter episode began (e.g., 82 represents the period from December 1982 through February 1983). The spatial correlation coefficients (ordinate) have been computed for the domain extending from 150°E eastward to 30°W and from 30° to 70°N.

pattern for MOGA is less than one-half (one-fifth) of the corresponding values for the GOGA and TOGA runs. The characteristic SST pattern associated with the MOGA mode (Fig. 11b) is reminiscent of the features in the North Pacific portion of the patterns deduced from observations (Fig. 3b) and the GOGA experiments (Fig. 5b). The pattern of the atmospheric response in Fig. 11a is considerably weaker than, and bears little spatial resemblance to, the accompanying patterns for GOGA and TOGA. The model atmosphere is evidently much more responsive to prescribed SST variability in the tropical Pacific than that in the North Pacific.

By virtue of the relationship between SST variations in the North Pacific and those in the tropical Pacific (Figs. 1–2), the expansion coefficients of the SST field associated with the MOGA mode exhibit a moderate temporal correlation with those associated with the GOGA and TOGA runs (see appropriate entries in Table 1). However, the correlations between the temporal variations of the atmospheric response in MOGA and those in GOGA and TOGA are considerably lower. The variability of the model responses in the four individual MOGA runs has been examined by computing the spatial correlation statistics R_s (not shown) in a manner analogous to that described in Fig. 7 for the GOGA runs. The scatter among the four MOGA experiments is generally wider than that in GOGA and TOGA.

6. Amplitude of atmospheric responses and dependence on polarity of SST forcing

The normalized coefficients in the heterogeneous correlation charts presented in the previous sections provide no information on the actual *amplitudes* of the anomalies constituting the principal SVD patterns. Furthermore, the SVD computations reveal only linear relationships between the atmospheric circulation and the SST changes—that is, as the polarity of the SST pattern is changed, the atmospheric pattern associated with a given SVD mode undergoes a sign reversal while preserving its spatial structure. In this section, we will examine the amplitude and degree of linearity of the atmospheric responses by constructing composite charts for the outstanding SST episodes.

We have used the periods during which the SST anomalies in both the tropical and North Pacific are prominent to construct the composite patterns. The identification of these periods is facilitated by the SVD analysis shown in Figs. 1–2. As explained in section 3a, a group of six warm winters with large, positive expansion coefficients for both the tropical Pacific SST field and the North Pacific SST field has been chosen (see labeled events in the upper-right quadrant of Fig. 2). Composite charts of these six winters will henceforth be referred to as the warm composites. Analogously, another group of six cold events with large, negative expansion coefficients (see lower-left quadrant of Fig. 2) serves as the basis for constructing the cold composite charts.

The warm (left panels) and cold (right panels) composite charts of the anomalous 515-mb height field simulated in each of the four TOGA runs are presented in Fig. 12. These anomalies are defined as departures

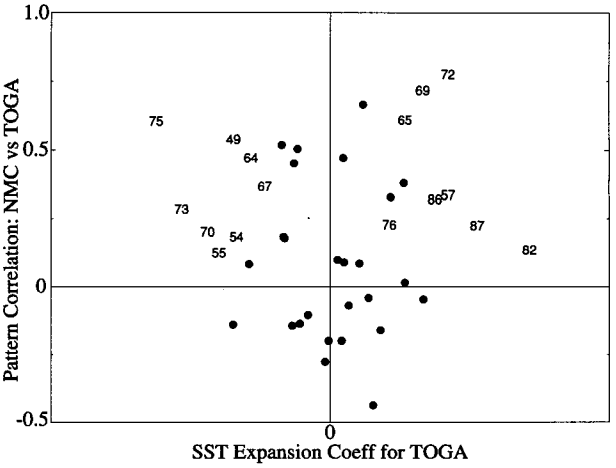

FIG. 10. As in Fig. 9 but for spatial correlation coefficients between the observed 500-mb height anomalies and the four-run ensemble average of the 515-mb height anomalies simulated in the TOGA experiment (ordinate) and the expansion coefficients of the SST field associated with the leading SVD mode in the TOGA experiment (abscissa).

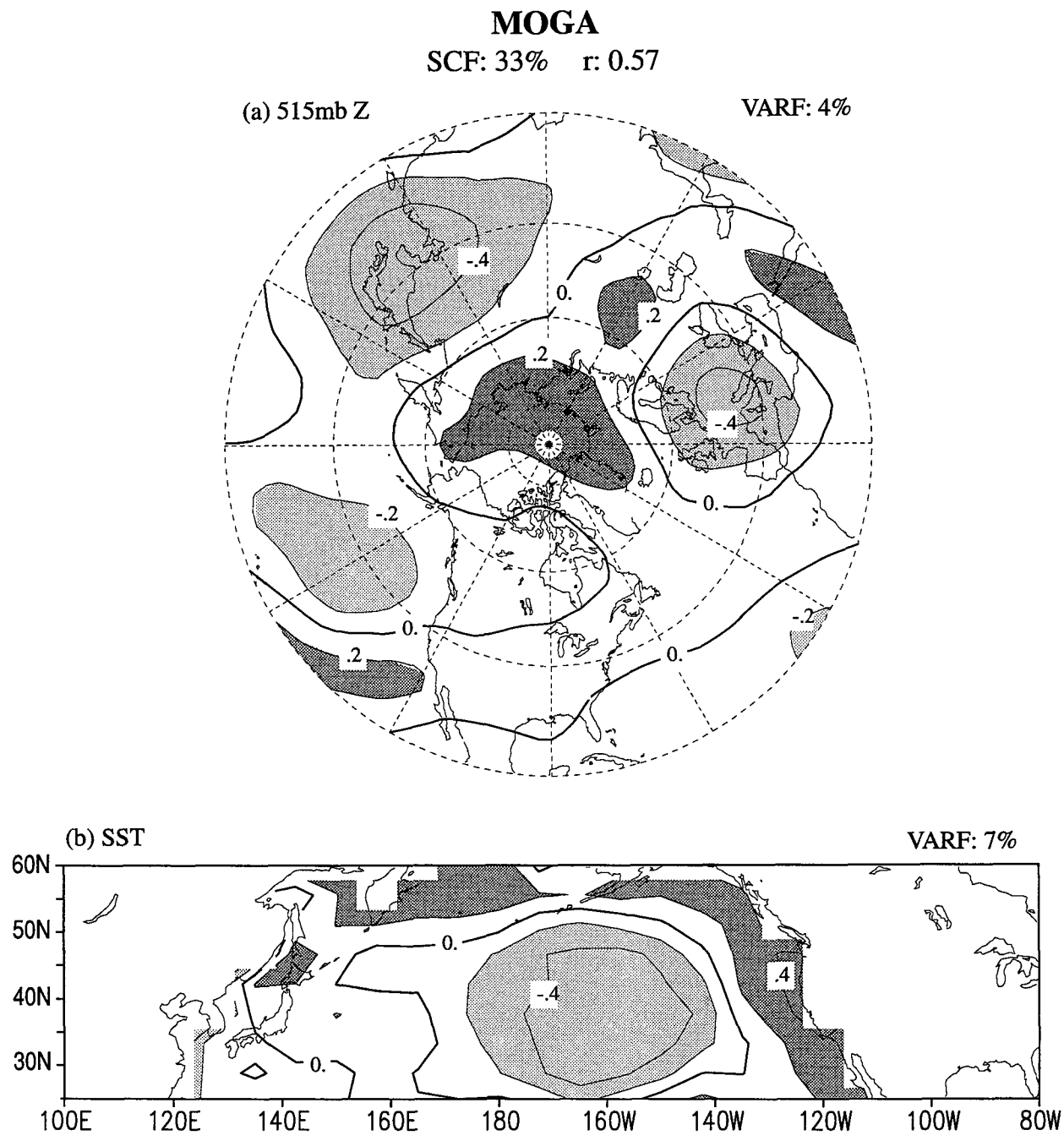

FIG. 11. As in Fig. 5 but for (a) the 515-mb height field simulated in the MOGA runs and (b) the SST forcing in the North Pacific.

of the local height values for a given winter in a given run from the 42-winter average in the same run. The corresponding patterns based on output from the four MOGA runs are shown in Fig. 13. In both figures, those anomalies with statistical significance exceeding the 90% and 95% levels, as determined using a two-tailed Student's *t*-test [see Chervin and Schneider (1976) for details of application] and assuming independent data samples for individual seasons, are indicated by light and dark stippling, respectively. The general characteristics of the composites based on the GOGA runs (not shown) are similar to those for the TOGA runs (Fig. 12), with comparable anomaly amplitudes, level of variability from one run to another, and degree of contrast between the warm and cold winters.

The composite patterns for the individual TOGA experiments (Fig. 12) exhibit a fair degree of reproducibility from one run to another, with the exception

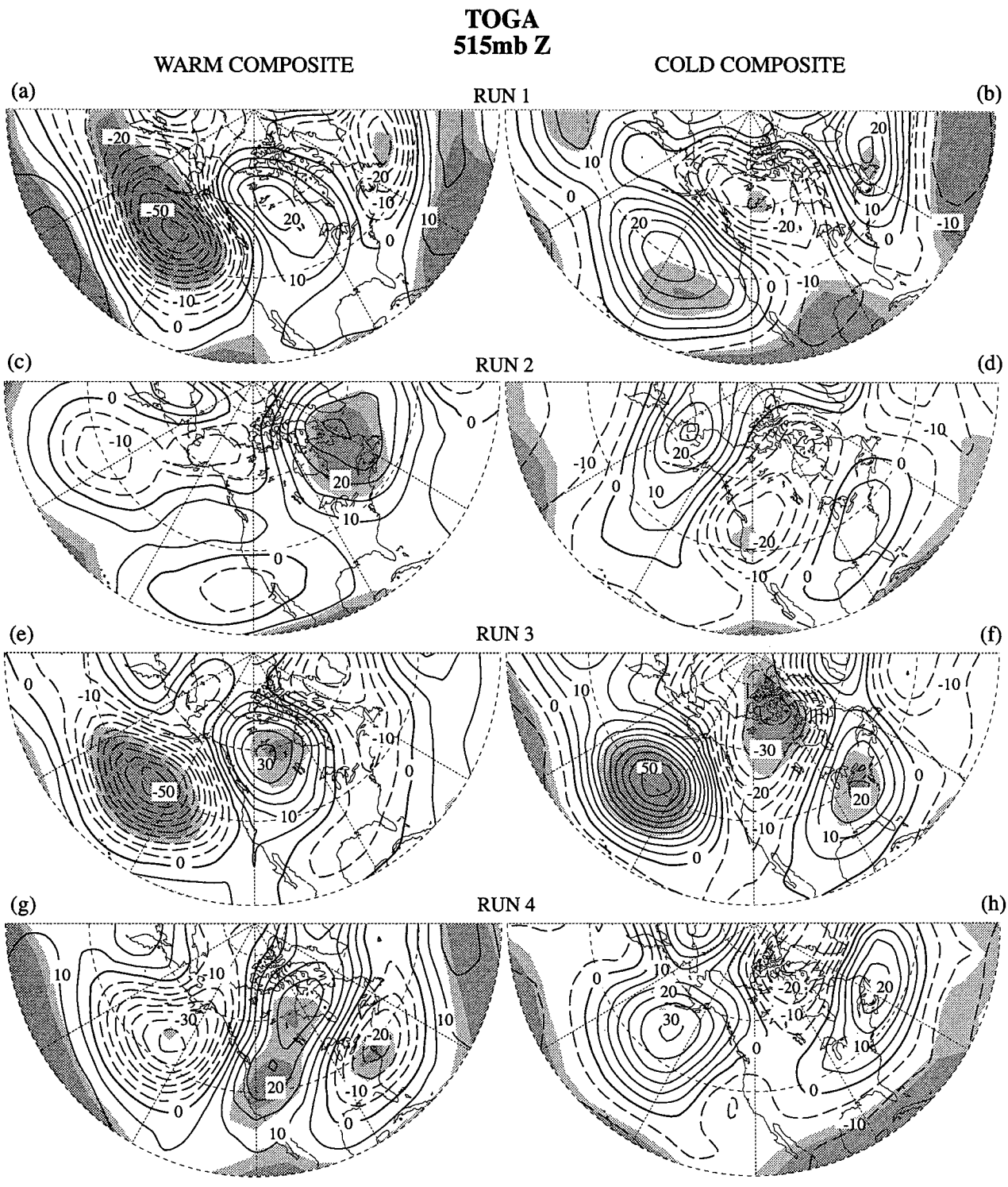

FIG. 12. Composite charts of the 515-mb height anomalies simulated in the four individual realizations of the TOGA experiment for the six winters with strong positive SST anomalies in the tropical Pacific and strong negative anomalies in the central North Pacific (the "warm" composites, see left panels) and for the six winters with strong negative SST anomalies in the tropical Pacific and strong positive anomalies in the central North Pacific (the "cold" composites, see right panels). The winters used in constructing these composites were selected on the basis of the expansion coefficients of the leading SVD mode for the SST fields in the tropical Pacific and North Pacific (see two-digit labels in Fig. 2). Solid (dashed) contours indicate positive (negative) anomalies. Contour interval: 5 m. Anomalies exceeding the thresholds for significance at the 90% and 95% levels are indicated by light and dark stippling, respectively.

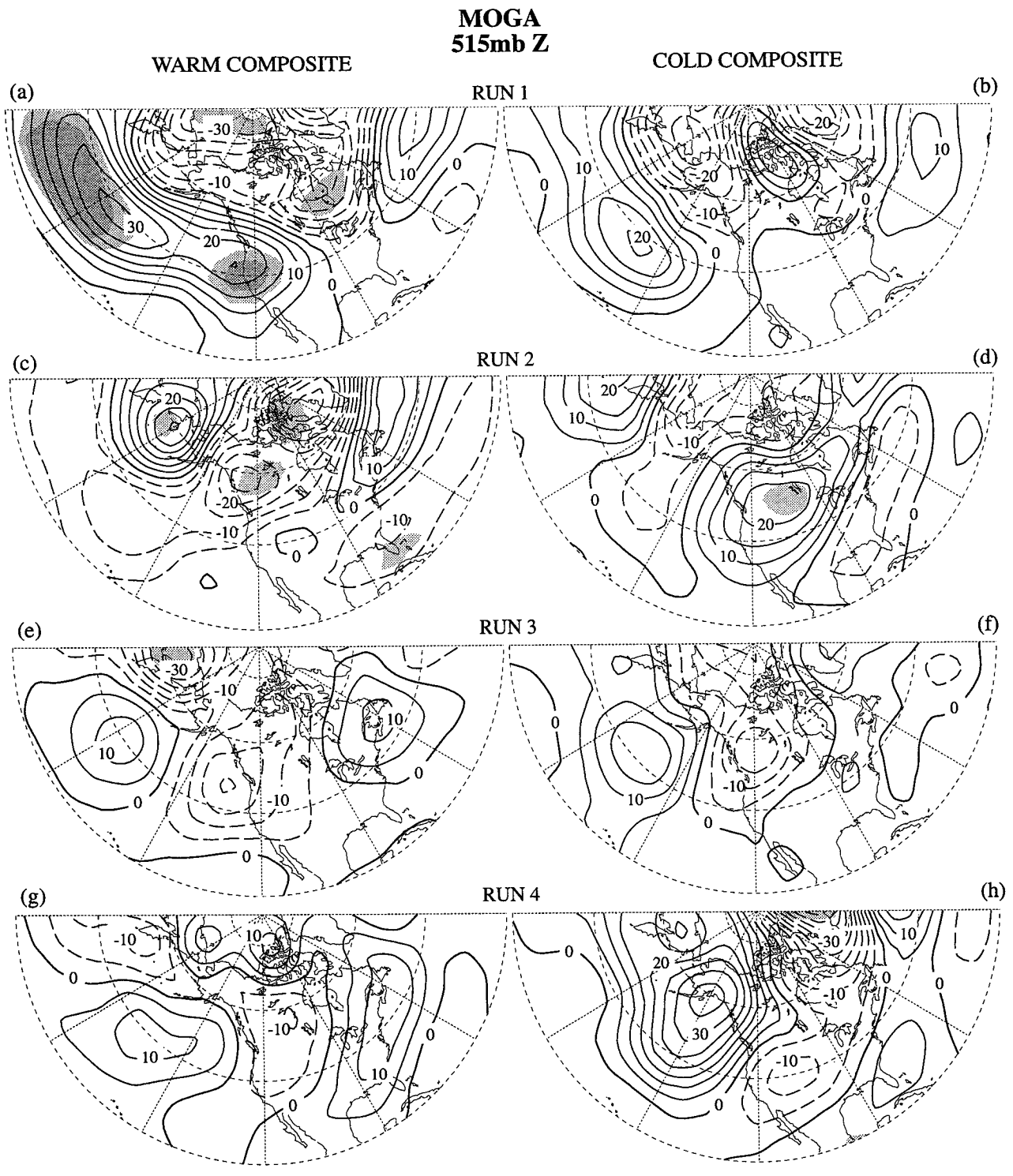

FIG. 13. As in Fig. 12 but for anomalies simulated in the four MOGA runs.

of the second integration (run 2). These maps generally bear a qualitative resemblance to the corresponding SVD pattern shown in Fig. 8a. In most of the composites, the main anomaly centers over the North Pacific, Canada, and the east coast of North America are significant at the 90% or 95% levels. In runs 1, 3, and 4, the polarities of the key features in the warm composite are opposite to those in the cold composite for

the same integration—that is, the model response is linear with respect to the polarity of the SST forcing in the tropical Pacific.

In comparison with the TOGA experiments, the MOGA integrations (Fig. 13) exhibit more variability from one run to another. The anomaly charts for the individual MOGA runs do not seem to bear any strong relationship with the corresponding SVD pattern in Fig. 11a. The amplitudes of most of the MOGA anomalies are lower than those in the TOGA composites. Only a few anomaly centers in Fig. 13 exceed the thresholds for 90% significance. Comparison between the left and right panels in the MOGA composites reveals that the height anomalies do not undergo a sign reversal from the warm winters to the cold winters. On the contrary, several anomaly centers in runs 1, 3, and 4 retain the *same* polarity in both the warm and cold composites. This model behavior has also been noted in previous GCM experiments analyzed by Pitcher et al. (1988) and Kushnir and Lau (1992).

The warm and cold composites based on the observed NMC analyses of the 500-mb height are shown in the top panels of Fig. 14. The amplitudes of some of the observed height anomalies in the warm composite tend to be higher than those in the cold composite. The corresponding patterns for the four-run ensemble average of the 515-mb height field simulated in the GOGA, TOGA, and MOGA experiments are displayed in the lower panels of the same figure. As in Figs. 12–13, anomalies exceeding the 90% and 95% significance levels are indicated here by stippling. The composites for NMC, GOGA, and TOGA in Fig. 14 share several common characteristics: their spatial structure is qualitatively similar, the significance levels of the anomaly centers are comparable, and the warm composites are opposite in polarity to the cold composites. There is, however, an important distinction between the NMC and model-simulated patterns: the observed anomalies are stronger than those in GOGA and TOGA by a factor of 2–3. Possible causes of the weaker model amplitudes include errors in the simulation of the climatological stationary waves and the absence of atmospheric feedbacks to the underlying ocean in the present experimental design. The ensemble mean MOGA patterns (bottom of Fig. 14) depict feeble and mostly insignificant model responses.

7. The "atmospheric bridge" between tropical Pacific forcing and worldwide SST anomalies

An important issue that remains to be addressed is the nature of the physical processes responsible for the observed occurrence of SST anomalies in the North Pacific (and elsewhere in the World Ocean) in conjunction with SST fluctuations in the tropical Pacific (e.g., see Figs. 1 and 3b). Considering the long timescales inherent in the basin-scale ocean circulation, it is unlikely that the linkages between concurrent SST changes in distant sites of the open ocean can be attributed to internal oceanic processes alone. Calling to mind the strong dependence of the North Pacific atmospheric circulation on tropical Pacific SST forcing (Fig. 8), one possible explanation for the basinwide SST anomaly pattern is that the variability of the North Pacific SST field is primarily driven by the local atmospheric circulation, which is in turn a remote response to SST variability in the tropical Pacific.

In the following computations, the expansion coefficients for the SST field associated with the leading SVD mode of air–sea coupling in the TOGA experiment (Fig. 8) have been used as the reference time series for the SST forcing in the tropical Pacific. Following the methodology outlined in Nakamura et al. (1987), temporal regression coefficients have been computed between the fluctuations of selected variables at individual grid points and this reference time series. The spatial distributions of the regression coefficients thus obtained will hereafter be referred to as regression patterns. The reference time series has been scaled by a constant factor, so that the resulting regression coefficients for the SST field in the central equatorial Pacific have amplitudes of approximately 1°C. Regression coefficients of a given variable versus the scaled reference time series therefore represent the typical magnitude and polarity of anomalies in that variable corresponding to ~+1°C of SST forcing in the equatorial Pacific.

a. Atmospheric influences on the surface heat fluxes

The regression patterns for the zonal and meridional components of the surface wind simulated in the TOGA experiment are presented in Fig. 15a using a vectorial format. The regression pattern for the sum of surface sensible and latent heat fluxes generated in TOGA is superposed on the same figure by stippling. Ensemble averages of the four TOGA runs have been used in computing all regression statistics displayed here. The sign convention adopted for the atmosphere–ocean energy exchange is such that positive anomalies correspond to above-normal flux from the atmosphere to the ocean (i.e., warming of the ocean surface) and vice versa. The sensible (latent) heat flux is parameterized in the GCM using bulk aerodynamic drag laws [see Gordon and Stern (1982), section 6b] and is proportional to the product of the instantaneous wind speed and the temperature (water vapor mixing ratio) difference between the ocean surface and the lowest atmospheric layer. Since air temperature fluctuations are positively correlated with changes in water vapor mixing ratio, the anomalies of sensible and latent heat fluxes tend to have the same polarity.

In the region of variable SST forcing over the tropical Pacific, Fig. 15a indicates that the TOGA experiment reproduces many of the familiar phenomena associated with the warm phase of observed ENSO events [e.g.,

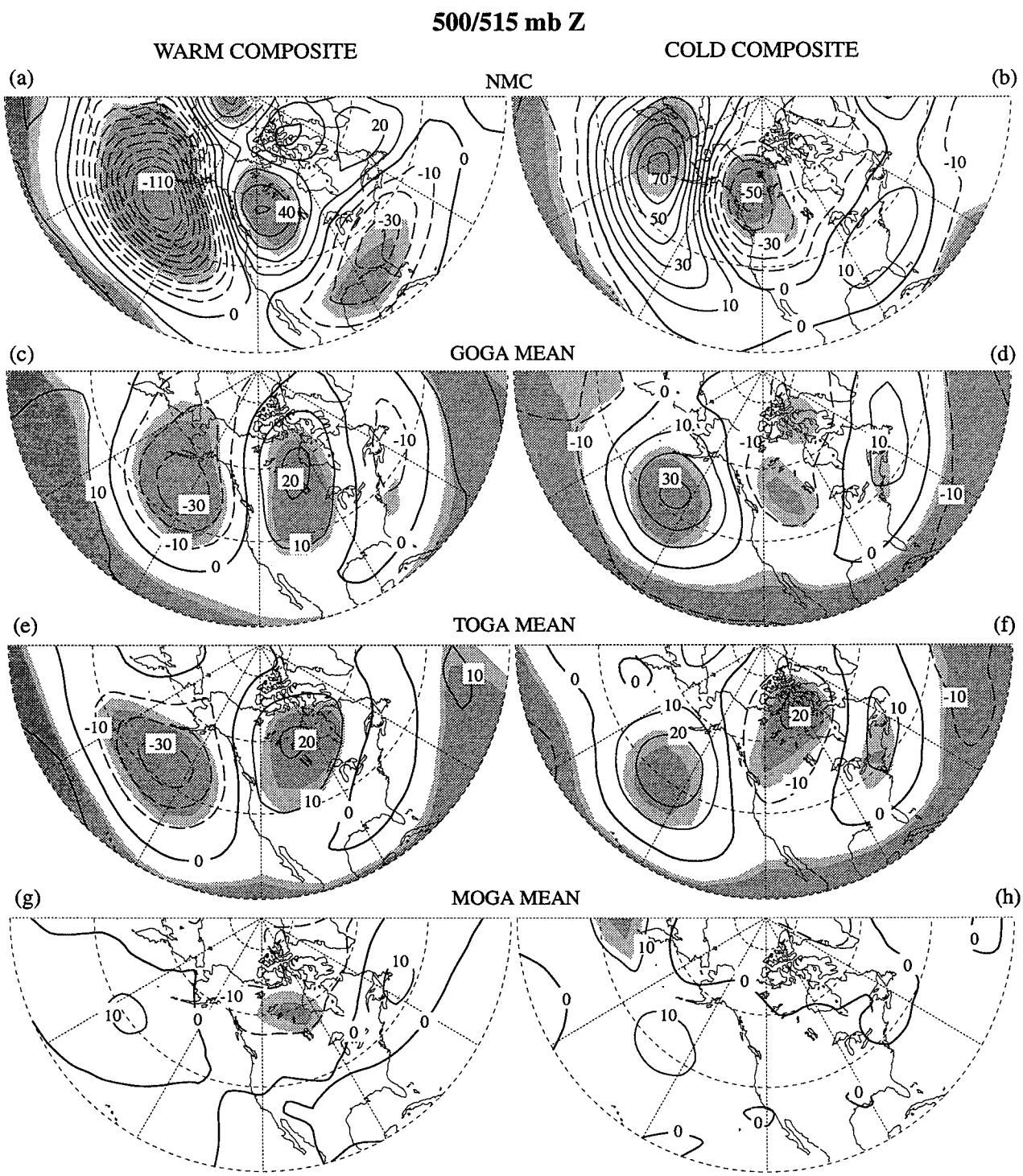

FIG. 14. As in Fig. 12 but for (a)–(b) observed 500-mb height anomalies and for four-run ensemble averages of the 515-mb height anomalies simulated in the (c)–(d) GOGA, (e)–(f) TOGA, and (g)–(h) MOGA experiments. Contour interval: 10 m.

see Rasmusson and Carpenter (1982), Fig. 21; Pan and Oort (1983), Fig. 9]. Particularly noteworthy are the anomalous westerlies and convergence of the surface flow in the central equatorial Pacific, as well as the cyclonic (clockwise) circulation anomaly south of the equator that is related to the eastward displacement of the South Pacific convergence zone. The heat flux pattern (stippling) in the forcing region is dominated by

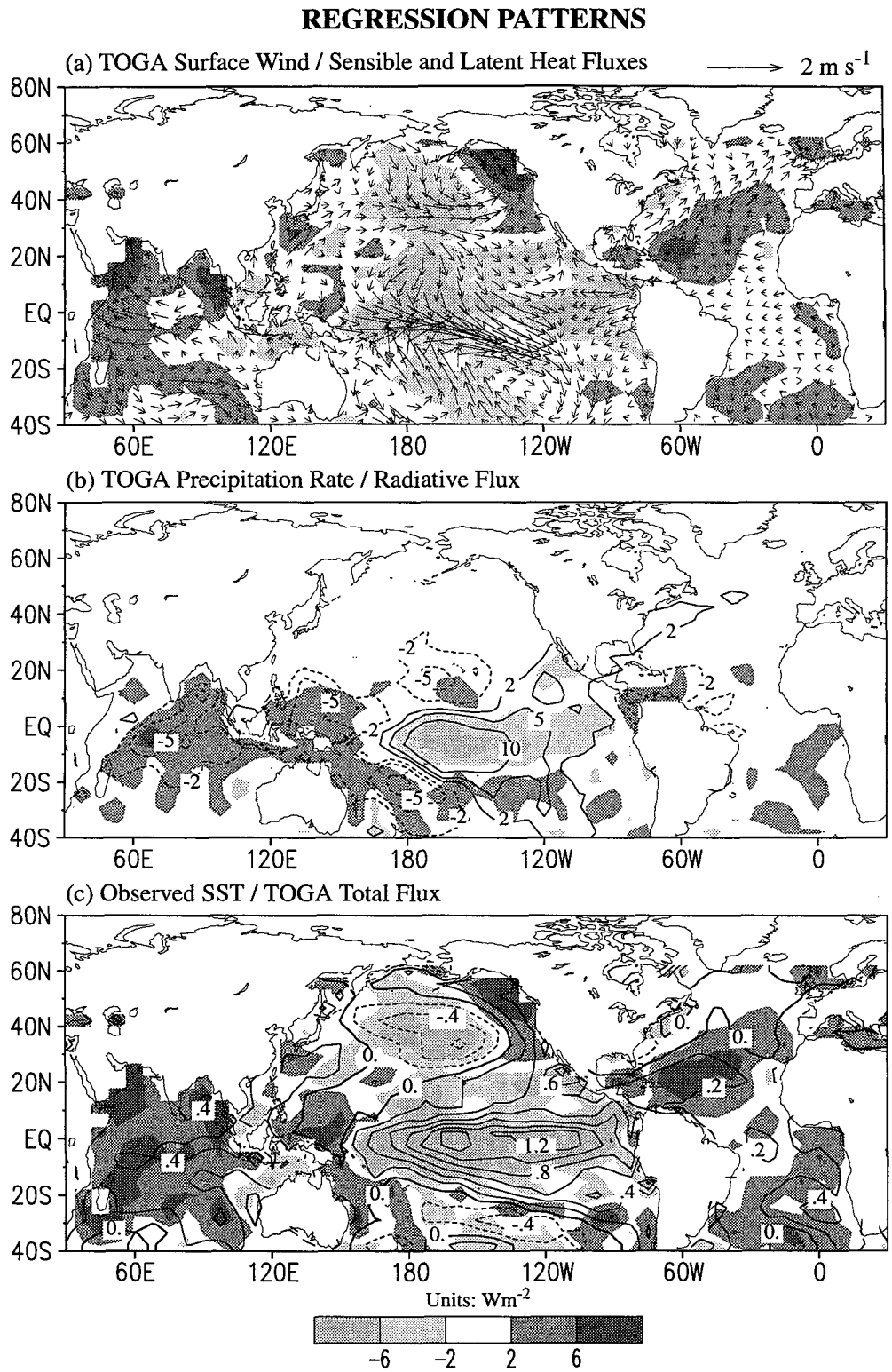

FIG. 15. Regression patterns of the scaled SST expansion coefficients associated with the leading SVD mode for the TOGA experiment versus (a) zonal and meridional components of the wind field at the lowest layer of the model atmosphere (vectors, see scale at upper right) and sum of latent and sensible heat fluxes from the atmosphere to the ocean (stippling), all simulated in the TOGA experiment; (b) precipitation rate (contours, units for contour labels: 10^{-2} cm d^{-1}) and net downward radiative flux at the ocean surface (stippling), all simulated in the TOGA experiment; and (c) observed SST (contours, interval: 0.2°C) and TOGA-generated

the elongated negative feature in the equatorial Pacific, indicating that the anomalous heat transfer across the air–sea interface acts to cool the surface waters during warm ENSO episodes. For 1°C of SST forcing, the typical magnitude of this flux anomaly is ~10 W m^{-2}, which would result in cooling of a mixed layer of 50-m depth by 1°C within ~8 months.

We now turn our attention to maritime locations outside of the tropical Pacific, where the thermal conditions have been fixed at their climatological values in the TOGA experiment. Figure 15a indicates that positive SST changes in the tropical Pacific are accompanied by an anomalous cyclonic surface circulation in the North Pacific, which is evidently linked to the concurrent height anomaly pattern at 515 mb (see Fig. 8a). The anomalous surface westerlies and northerlies in the central North Pacific are collocated with negative flux anomalies, whereas the enhanced southerlies over the Gulf of Alaska are associated with positive changes in the heat fluxes. The passage of cold and dry air masses over a maritime site associated with anomalous northerly surface flows tends to enhance the loss of heat and water vapor from the underlying, relatively warm ocean surface, thus lowering the local SST. Conversely, the invasion of warm and moist air masses accompanying intensified surface southerlies leads to positive SST anomalies. The strengthening of the climatological westerlies along the 30°–40°N zone tends to enhance the upward heat fluxes from the ocean surface, thus lowering the SST. Similar relationships between the near-surface atmospheric circulation and surface flux fields in the northern oceans have been reported in an observational study by Cayan (1992a). The magnitudes of these extratropical flux anomalies (~10 W m^{-2} per °C of SST forcing in the tropical Pacific) are comparable to those in the forcing region itself.

In the Atlantic basin, the most prominent circulation feature in Fig. 15a is the belt of anomalous surface southwesterlies extending from ~25° to ~55°N. The cooling of the surface ocean due to strengthening of the climatological westerlies counteracts with oceanic warming due to advection of warm air masses from the western subtropical Atlantic. As a result, the southwesterly anomalies are not accompanied by strong changes in the heat fluxes. There is an extensive region of positive flux anomaly in the western and central subtropical North Atlantic between ~10° and ~30°N. The prevalent southwesterly anomalies in the western portion of this region lead to weakening of the local climatological northeasterly trades.

In the Indian Ocean, the waters in the eastern portion of the Bay of Bengal and off the coasts of the Arabian peninsula are characterized by positive heat flux anomalies. The surface wind changes in both regions have an onshore component and are indicative of a weakened northeasterly or northerly (offshore) wintertime monsoon circulation. These circulation anomalies would lead to a reduction in the heat loss from the ocean (i.e., warming).

b. Atmospheric influences on the surface radiative fluxes

The regression patterns of the precipitation rate and net radiative flux into the ocean for the TOGA runs are presented in Fig. 15b using contours and stippling, respectively. Over the tropical oceans, the magnitude of the fluctuations in shortwave flux at the surface is typically larger than that of the longwave contribution by a factor of 3–4, so that the net surface flux is dominated by changes in the shortwave component (e.g., see Ramanathan 1987). Variations in the intensity of solar radiation arriving at the ocean surface are mainly controlled by the amount of cloud cover aloft, which is correlated with the occurrence of precipitation. These relationships are substantiated by the notable spatial correspondence between regression patterns for the net radiative flux and precipitation rate (shown in Fig. 15b) and for the frequency of cloud cover (not shown, qualitatively similar to the precipitation pattern). For instance, the simulated precipitation over the equatorial central and eastern Pacific is enhanced during warm episodes, thus leading to increased local cloud cover and reduced net radiative flux. At the same time, the suppression of convective activity over the equatorial western Pacific and central Indian Oceans is accompanied by reduced cloud cover, increased net radiative flux, and warming of the local ocean surface. The typical amplitudes of the net radiative flux anomalies (~6 W m^{-2} per °C of SST forcing in the tropical Pacific) are comparable to those of local changes in latent and sensible heat fluxes (Fig. 15a). The pattern in Fig. 15b does not show any notable anomalies of radiative fluxes in the northern extratropics, thus indicating that fluctuations in midlatitude air–sea exchanges are mainly determined by changes in latent and sensible heat fluxes.

---

sum of downward latent heat, sensible heat, and radiative fluxes (stippling). All TOGA data are based on averages over the four different realizations for individual northern winters. Solid (dashed) contours indicate positive (negative) values. A common scale [see bottom of (c)] has been used to present the stippling patterns for the surface energy fluxes in all three panels. Heavy and light stippling indicate positive and negative flux anomalies, which would lead to oceanic warming and cooling, respectively. The SST expansion coefficients have been scaled by a constant factor, so that the regression values shown here give the typical amplitudes of various anomalies for +1°C of SST forcing in the central tropical Pacific.

c. *Local relationships between simulated surface fluxes and observed SST anomalies*

We proceed to evaluate the extent to which *observed* SST changes might be linked to local surface fluxes induced by the *simulated* atmospheric response to tropical Pacific forcing. The regression patterns for the observed SST field and the sum of latent heat, sensible heat, and radiative fluxes simulated in TOGA are displayed in Fig. 15c using contours and stippling, respectively. Within the forcing region in the tropical Pacific, the surface fluxes act to cool the ocean surface when the local SST is above normal, and vice versa. The fluxes hence constitute a dissipative mechanism for the imposed SST forcing in this region, as was previously noted by Barnett et al. (1991). A completely different surface flux–SST relationship is discerned outside the forcing region, with the simulated surface fluxes acting to warm the underlying ocean at those locations where positive SST anomalies are observed, and vice versa. Particularly noteworthy is the collocation of the negative surface flux and cold SST anomalies in the central North Pacific, as well as the association of positive flux and warm SST changes in the eastern North Pacific, subtropical North Atlantic, Bay of Bengal, and the equatorial Indian Ocean. As pointed out earlier in this section, the surface flux anomalies at the above maritime sites result from pronounced changes either in the local circulation at sea level or in the amount of cloud cover.

The results in Fig. 15 support the hypothesis that the observed SST changes outside the tropical Pacific are related to oceanic responses to atmospheric processes, which are in turn influenced by SST conditions in the forcing region. Considering that no information on the SST variability beyond the tropical Pacific has been provided to the model atmosphere in the TOGA experiment, the spatial correspondence between the two independent fields in Fig. 15c (i.e., the observed SST and the model-simulated surface flux) is rather remarkable. The importance of latent and sensible heat fluxes in driving the SST field over the northern oceans has been confirmed by the observations presented in Cayan (1992b). In addition to the heat and radiative fluxes examined here, other processes might also contribute to local air–sea interaction, among which are mechanical stirring of the oceanic mixed layer due to momentum transfer from the overlying atmosphere and negative feedback of SST changes on surface fluxes in a two-way coupled system [e.g., see Alexander (1992a), section 4a].

8. Discussion

a. *Comparison with other studies*

The research objectives and experimental design of the study performed independently by Graham et al. (1994) are very similar to those of our work. They have analyzed the output from single realizations of three experiments analogous to GOGA, TOGA, and MOGA for the 1970–88 period. They pointed out that the output from the model run subjected only to tropical SST forcing compares most favorably with the observations, whereas the response to extratropical SST is much weaker and less systematic. As in our study, the amplitude of simulated height anomalies obtained by Graham et al. is weaker than the observed values, although the degree of underestimation in their experiments is less severe than that reported here. Graham et al. (see their Table 1) noted that the pattern correlation between the model-generated height anomalies and the observations is higher (lower) when the tropical SST is above (below) normal. This relationship between model performance and polarity of the tropical SST forcing is not evident in our TOGA results (see our Fig. 10). The sensitivity of a model atmosphere to localized SST anomalies at three tropical and two extratropical sites has been evaluated by Ferranti et al. (1994). These authors also concluded that the model response to SST anomalies in the central and eastern tropical Pacific is much stronger and more reproducible than the response to extratropical forcing.

The proposition that the atmospheric response to tropical ENSO phenomena plays a significant role in forcing SST anomalies in the North Pacific has been tested directly by numerical experimentation. Alexander (1990) examined the surface energy flux and wind stress fields from an atmospheric GCM experiment that has been subjected to warm SST forcing in the tropical Pacific. He then used these surface fields to drive a mixed-layer ocean model of the North Pacific. The midlatitude SST anomalies thus obtained are in good agreement with the observed SST pattern (see his Fig. 4). The additional model analyses by Alexander (1992a,b) delineate the effects of various feedback processes on the formation of SST anomalies in the North Pacific during ENSO. Luksch and von Storch (1992) prescribed an anomalous, ENSO-related wind forcing over an ocean GCM of the Pacific basin and obtained an oceanic response in the North Pacific that bears a considerable resemblance to the observed SST pattern (see their Fig. 15). They further noted that the atmospheric forcing associated with ENSO explains as much as half of the variance of the simulated SST field in the North Pacific.

b. *Discrepancies with an earlier GOGA run*

Lau and Nath (1990, hereafter LN90) have examined the output from a single realization of a 30-yr experiment (1950–79) similar to the GOGA integration described here. The earlier model run was conducted using essentially the same GCM, except for the treatment of the cloud field, more details of which will be provided later in this subsection. Noting that the atmospheric fluctuations in the LN90 simulation exhibit a promi-

nent zonally symmetric component, the diagnosis in that earlier study was mostly performed on model output from which the zonal mean values had been removed. By applying analysis techniques that are different from those used here, LN90 reported that the zonally asymmetric atmospheric mode in the Pacific/North American sector exhibits a higher correlation with the SST changes in the North Pacific than with those in the tropical Pacific (see their Figs. 2b and 3b). This finding is at odds with the evidence presented here (and with modeling studies by other investigators cited above), which indicates that the wavelike response of the model atmosphere is more sensitive to SST anomalies in the tropical Pacific.

To evaluate how the above discrepancy might be attributed to differences in analysis procedures being used in the two studies, we have subjected the model output for 515-mb height from LN90 (with the zonal mean values retained) and the near-global SST forcing to the same SVD analysis performed here. The heterogeneous correlation chart for the SST field associated with the leading mode in LN90 (not shown, SCF = 44%, $r = 0.80$, VARF = 12%) resembles its counterpart for the GOGA runs described here (see Fig. 5b). The accompanying chart for 515-mb height in LN90 (VARF = 11%) resembles the ubiquitous, zonally symmetric pattern mentioned in the preceding paragraph. Hence, the tropical SST anomalies (which dominate the global SST field) in the earlier experiment do not play a significant role in forcing the wavelike circulation pattern in the North Pacific/North American region.

A significant distinction between LN90 and the present work is the handling of cloud cover in the GCM. The cloud amount was prescribed as a function of latitude and height in LN90, whereas the current investigation is based on a model with a cloud prediction scheme. To assess the impact of cloud cover on the results presented here, a single 43-yr GOGA integration has been repeated using the same GCM for the present study but with the cloud amount being fixed at the observed, zonally averaged climatological values. A SVD analysis has been performed on the 515-mb height and near-global SST fields for this "fixed cloud" experiment. This analysis yields a lower SCF (56%, versus 60%–65% for the four individual GOGA runs with variable clouds) and a lower VARF for the height field (10%, versus ~15% for runs with predicted clouds). Otherwise, the fixed cloud experiment reproduces many of the atmosphere–ocean relationships noted in model runs with predicted clouds. The cloud effects therefore provide only a partial explanation for the weak connection between the zonally asymmetric component of the extratropical flow and the tropical SST changes in the fixed cloud experiment examined by LN90.

The sampling fluctuations in the ensemble of model responses to a given SST scenario could also contribute to the discrepancy between LN90 and the present study. An appreciation of the degree of variability in the responses in different model runs may be gained by inspecting Figs. 7, 12, and 13. For the TOGA experiment, it is worth noting that the results for run 2 (Figs. 12c and 12d) are noticeably different from the other three runs. The response in the LN90 experiment could well be another such "outlier" among the population of realizable model responses. A quantitative assessment of the characteristics of these sampling fluctuations would require a much larger set of integrations than the four runs attempted here.

A more definitive account of all the causes for the differences between the results in LN90 and the present work remains elusive at this time. Nonetheless, the weight of the evidence accumulated thus far argues strongly for the importance of tropical Pacific SST anomalies in forcing anomalous midlatitude atmospheric patterns, with the impact of midlatitude SST changes on the atmospheric circulation being comparatively weaker. The credibility of these inferences is enhanced by the more comprehensive suite of experiments conducted for the current study, with explicit separation of the atmospheric effects due to tropical and extratropical SST forcing and with multiple realizations of the model response to SST changes in a given region. The findings of independent modeling studies by other authors (see previous subsection) lend further support to the conclusions drawn in the present work.

c. *Scope for future investigations*

The results presented here indicate that substantial differences exist between the model responses during specific events in the 1946–88 period, both in terms of the amplitude of the atmospheric anomalies (see Figs. 6 and 7) and the degree of spatial resemblance with the corresponding observations (Fig. 10). The variability among events may be explored further by diagnosing the simulated and observed space–time evolution of each anomalous episode and the relative roles of various physical processes linking the tropical forcing to the midlatitude anomalies during individual events.

Our attention has thus far been exclusively devoted to simulated phenomena during the December–February period. Since the timing of the development of the observed SST anomaly pattern in relation to the climatological seasonal cycle is known to differ from one specific event to another (e.g., see Rasmusson and Wallace 1983), it would be of interest to examine the seasonal dependence of both the observed and simulated air–sea coupling in greater detail.

The observed and simulated atmosphere–ocean systems exhibit pronounced variability on both interannual and interdecadal timescales (Figs. 4 and 6). Diagnoses of the observed atmosphere–ocean variability in the North Atlantic by Kushnir (1994) and the Pacific

basin by Trenberth and Hurrell (1994) suggest that the physical mechanisms relevant to interannual phenomena could be quite different from those governing interdecadal changes. In particular, fluctuations in the oceanic circulation could influence the SST and atmospheric climate on decadal timescales. In view of the current interest in the natural and anthropogenic causes of low-frequency variability of the climate system, it would be interesting to reexamine the output from the model runs described here with these issues in mind.

The potential role of the global-scale atmospheric circulation in communicating ENSO signals in the tropical Pacific to other parts of the World Ocean (see section 7) has important implications for our understanding of the causal factors of atmosphere–ocean variability in different locations and for advancing our skill in predicting the coupled system on seasonal timescales. Alexander (1990, 1992a,b) and Luksch and von Storch (1992) have begun to address this issue in greater detail by using coupled or uncoupled air–sea models of varying degrees of complexity. These studies have mostly been concerned with the reaction of the wintertime SST field in the North Pacific to ENSO forcing originating from the tropical Pacific. Since the correlations between observed SST anomalies in the tropical Pacific and those in the Atlantic and Indian Oceans are just as strong as the correlations with the North Pacific (see Fig. 3b), much remains to be done to identify the mechanisms responsible for the links between different ocean basins. Diagnosis of the TOGA output (section 7) suggests that cloud/radiation processes and variations of the monsoonal flow could contribute to SST changes in the Indian Ocean. The validity of these model results needs to be substantiated by observational analyses. The strong influences of the annual cycle on ocean mixed-layer dynamics call for an extended study of the "atmospheric bridge" connecting various maritime sites in seasons other than winter. In view of the well-defined relationships between the seasonal atmospheric anomalies and the preferred trajectories of cyclone-scale disturbances ("storm tracks") over the oceans (e.g., see Lau 1988), the potential role of the latter features in establishing this atmospheric bridge needs to be assessed further. The myriad feedback processes involved in planetary-scale air–sea interactions would ultimately have to be examined using global and fully coupled atmosphere–ocean GCMs.

Acknowledgments. We would like to thank Drs. I. M. Held and J. M. Wallace for their encouragement and for sharing their insights throughout the course of this study. We are grateful to Dr. A. H. Oort for providing the observed SST analyses and to Drs. T. P. Barnett and N. E. Graham for drawing our attention to their recent works on this problem. Drs. Held, Oort, J. R. Lanzante, and H. Nakamura have examined an earlier version of the manuscript and have made numerous helpful suggestions for improving it. This project is part of a NOAA/Universities collaborative effort aimed at understanding atmospheric variability associated with boundary forcings and is supported by the NOAA Climate and Global Change Program.

REFERENCES

Alexander, M. A., 1990: Simulation of the response of the North Pacific Ocean to the anomalous atmospheric circulation associated with El Niño. *Climate Dyn.*, **5**, 53–65.

——, 1992a: Midlatitude atmosphere–ocean interaction during El Niño. Part I: The North Pacific Ocean. *J. Climate*, **5**, 944–958.

——, 1992b: Midlatitude atmosphere–ocean interaction during El Niño. Part II: The Northern Hemisphere atmosphere. *J. Climate*, **5**, 959–972.

Barnett, T. P., M. Latif, E. Kirk, and E. Roeckner, 1991: On ENSO physics. *J. Climate*, **4**, 487–515.

Barnston, A. G., and R. E. Livezey, 1987: Classification, seasonality, and persistence of low-frequency atmospheric circulation patterns. *Mon. Wea. Rev.*, **115**, 1083–1126.

Blackmon, M. L., J. E. Geisler, and E. J. Pitcher, 1983: A general circulation model study of January climate anomaly patterns associated with interannual variation of equatorial Pacific sea surface temperatures. *J. Atmos. Sci.*, **40**, 1410–1425.

Bretherton, C. S., C. Smith, and J. M. Wallace, 1992: An intercomparison of methods for finding coupled patterns in climate data. *J. Climate*, **5**, 541–560.

Cayan, D. R., 1992a: Latent and sensible heat flux anomalies over the northern oceans: The connection to monthly atmospheric circulation. *J. Climate*, **5**, 354–369.

——, 1992b: Latent and sensible heat flux anomalies over the northern oceans: Driving the sea surface temperature. *J. Phys. Oceanogr.*, **22**, 859–881.

Chervin, R. M., and S. H. Schneider, 1976: On determining the statistical significance of climate experiments with general circulation models. *J. Atmos. Sci.*, **33**, 405–412.

Davis, R. E., 1976: Predictability of sea surface temperature and sea level pressure anomalies over the North Pacific Ocean. *J. Phys. Oceanogr.*, **6**, 249–266.

Ferranti, L., F. Molteni, and T. N. Palmer, 1994: Impact of localised tropical and extratropical SST anomalies in ensembles of seasonal GCM integrations. *Quart. J. Roy. Meteor. Soc.*, **120**, in press.

Gordon, C. T., and W. F. Stern, 1982: A description of the GFDL global spectral model. *Mon. Wea. Rev.*, **110**, 625–644.

Graham, N. E., T. P. Barnett, R. Wilde, U. Schlese, and L. Bengtsson, 1994: On the roles of tropical and midlatitude SSTs in forcing interannual to interdecadal variability in the winter Northern Hemisphere circulation. *J. Climate*, **7**(9), in press.

Horel, J. D., and J. M. Wallace, 1981: Planetary scale atmospheric phenomena associated with the Southern Oscillation. *Mon. Wea. Rev.*, **109**, 813–829.

Hoskins, B. J., and D. J. Karoly, 1981: The steady linear response of a spherical atmosphere to thermal and orographic forcing. *J. Atmos. Sci.*, **38**, 1179–1196.

Hsiung, J., and R. E. Newell, 1983: The principal nonseasonal modes of variation of global sea surface temperature. *J. Phys. Oceanogr.*, **13**, 1957–1967.

Kushnir, Y., 1994: Interdecadal variations in North Atlantic sea surface temperature and associated atmospheric conditions. *J. Climate*, **7**, 141–157.

——, and N.-C. Lau, 1992: The general circulation model response to a North Pacific SST anomaly: Dependence on time scale and pattern polarity. *J. Climate*, **5**, 271–283.

Lau, N.-C., 1985: Modeling the seasonal dependence of the atmospheric response to observed El Niños in 1962–76. *Mon. Wea. Rev.*, **113**, 1970–1996.

——, 1988: Variability of the observed midlatitude storm tracks in relation to low-frequency changes in the circulation pattern. *J. Atmos. Sci.*, **45**, 2718–2743.

——, and M. J. Nath, 1990: A general circulation model study of the atmospheric response to extratropical SST anomalies observed in 1950–79. *J. Climate*, **9**, 965–989.

Luksch, U., and H. von Storch, 1992: Modeling the low-frequency sea surface temperature variability in the North Pacific. *J. Climate*, **5**, 893–906.

Nakamura, H., M. Tanaka, and J. M. Wallace, 1987: Horizontal structure and energetics of Northern Hemisphere wintertime teleconnection patterns. *J. Atmos. Sci.*, **44**, 3377–3391.

Namias, J., 1969: Seasonal interactions between the North Pacific Ocean and the atmosphere during the 1960s. *Mon. Wea. Rev.*, **97**, 173–192.

Nitta, T., and S. Yamada, 1989: Recent warming of tropical sea surface temperature and its relationship to the Northern Hemisphere circulation. *J. Meteor. Soc. Japan*, **67**, 375–383.

Palmer, T. N., and Z.-B. Sun, 1985: A modelling and observational study of the relationship between sea surface temperature in the north-west Atlantic and the atmospheric general circulation. *Quart. J. Roy. Meteor. Soc.*, **111**, 947–975.

Pan, Y. H., and A. H. Oort, 1983: Global climate variations connected with sea surface temperature anomalies in the eastern equatorial Pacific Ocean for the 1958–73 period. *Mon. Wea. Rev.*, **111**, 1244–1258.

——, and ——, 1990: Correlation analyses between sea surface temperature anomalies in the eastern equatorial Pacific and the World Ocean. *Climate Dyn.*, **4**, 191–205.

Pitcher, E. J., M. L. Blackmon, G. T. Bates, and S. Muñoz, 1988: The effect of North Pacific sea surface temperature anomalies on the January climate of a general circulation model. *J. Atmos. Sci.*, **45**, 173–188.

Ramanathan, V., 1987: The role of earth radiation budget studies in climate and general circulation research. *J. Geophys. Res.*, **92**, 4075–4095.

Rasmusson, E. M., and T. H. Carpenter, 1982: Variations in tropical sea surface temperature and surface wind fields associated with the Southern Oscillation/El Niño. *Mon. Wea. Rev.*, **110**, 354–384.

——, and J. M. Wallace, 1983: Meteorological aspects of the El Niño/Southern Oscillation. *Science*, **222**, 1195–1202.

Ratcliffe, R. A. S., and R. Murray, 1970: New lag associations between North Atlantic sea temperature and European pressure applied to long-range weather forecasting. *Quart. J. Roy. Meteor. Soc.*, **96**, 226–246.

Sardeshmukh, P. D., and B. J. Hoskins, 1988: The generation of global rotational flow by steady idealized tropical divergence. *J. Atmos. Sci.*, **45**, 1228–1252.

Shukla, J., and J. M. Wallace, 1983: Numerical simulation of the atmospheric response to equatorial Pacific sea surface temperature anomalies. *J. Atmos. Sci.*, **40**, 1613–1630.

Ting, M., and N.-C. Lau, 1993: A diagnostic and modeling study of the monthly mean wintertime anomalies appearing in an 100-year GCM experiment. *J. Atmos. Sci.*, **50**, 2845–2867.

Trenberth, K. E., 1990: Recent observed interdecadal climate changes in the Northern Hemisphere. *Bull. Amer. Meteor. Soc.*, **71**, 988–993.

——, and J. W. Hurrell, 1994: Decadal atmosphere–ocean variations in the Pacific. *Climate Dyn.*, **9**, 303–319.

van Loon, H., and R. A. Madden, 1981: The Southern Oscillation. Part I: Global associations with pressure and temperature in northern winter. *Mon. Wea. Rev.*, **109**, 1150–1162.

Wallace, J. M., and D. S. Gutzler, 1981: Teleconnections in the geopotential height field during the Northern Hemisphere winter. *Mon. Wea. Rev.*, **109**, 784–812.

——, C. Smith, and Q.-R. Jiang, 1990: Spatial patterns of atmosphere/ocean interaction in the northern winter. *J. Climate*, **3**, 990–998.

——, ——, and C. S. Bretherton, 1992: Singular value decomposition of wintertime sea surface temperature and 500-mb height anomalies. *J. Climate*, **5**, 561–576.

Weare, B. C., A. Navato, and R. E. Newell, 1976: Empirical orthogonal analysis of Pacific Ocean sea surface temperatures. *J. Phys. Oceanogr.*, **6**, 671–678.

Wetherald, R. T., and S. Manabe, 1988: Cloud feedback processes in a general circulation model. *J. Atmos. Sci.*, **45**, 1397–1415.

Woodruff, S. D., R. J. Slutz, R. L. Jenne, and P. M. Steurer, 1987: A comprehensive ocean–atmosphere data set. *Bull. Amer. Meteor. Soc.*, **68**, 1239–1250.